Title
Cell Traction Force Measurement Platforms

Author
Tan, Xing Haw Marvin

Publication Date
2021

Peer reviewed|Thesis/dissertation

UNIVERSITY OF CALIFORNIA

Los Angeles

Cell Traction Force Measurement Platforms

A dissertation submitted in partial satisfaction of the

requirements for the degree Doctor of Philosophy

in Bioengineering

by

Xing Haw Marvin Tan

2021

ABSTRACT OF THE DISSERTATION

Cell Traction Force Measurement Platforms

by

Xing Haw Marvin Tan

Doctor of Philosophy in Bioengineering

University of California, Los Angeles, 2021

Professor Michael Alan Teitell, Co-Chair

Professor Pei-Yu Chiou, Co-Chair

Mechanical properties of cells and tissues play important roles in governing the behaviors of biological systems. Technologies for high-throughput quantification of multicellular mechanical responses provide fundamental insights into biological processes and are valuable in clinical applications, such as for diagnostics or drug discovery. Here, we present two different types of optical technologies for cell traction stress measurements over large fields-of-view of 0.6 mm^2 and 13 mm^2. The first type uses gold micro-disks or gold nanoparticles to scatter light strongly, thereby giving a high signal-to-noise ratio under dark field microscopy. This enables low magnification (10x) and low numerical aperture objective lenses to be used, hence greatly increasing the field-of-view over prior works whilst preserving sub-cellular resolution. The

second type of optical technology are Diffractive Optical Tracers (DOT) for direct measurement of mechanical waves propagating over 10,000 interconnected cells with sub-cellular resolution over a field-of-view of 13 mm^2. Dynamic mechanical stress distribution can be extracted from the color spectra recorded by an array of diffractive micromirrors embedded in an elastomer substrate. DOT provides mechanical information of individual cells, mechanical interactions between cells, patterns of traction stresses across multiple cells, and potential synergistic, antagonistic force generating activities. As a testbed example, we have applied DOT to measure the mechanical beating waves propagating through a syncytium of cardiomyocytes, quantify the dynamic contraction and relaxation forces of normal and phenylephrine treated neonatal rat ventricular myocytes (NRVMs). DOT can also be used to study other cell types including those derived from stem cells, cancer cells, macrophages, epithelial and endothelial cells for broad applications.

The dissertation of Xing Haw Marvin Tan is approved.

Tsu-Chin Tsao

Amy Catherine Rowat

Michael Alan Teitell, Committee Co-Chair

Pei-Yu Chiou, Committee Co-Chair

University of California, Los Angeles

2021

TABLE OF CONTENTS

Chapter 5

LIST OF FIGURES

ACKNOWLEDGEMENTS

First, I would like to thank my advisor Professor Pei-Yu Chiou for his guidance and support in my study and research during the past five years. His passion for technical innovation has motivated me to embrace challenges and open myself up to new opportunities. I would also like to thank Professor Michael Alan Teitell for countless discussion with invaluable insight and knowledge in the fields of biological studies. I thank Professor Amy Catherine Rowat and Professor Tsu-Chin Tsao for serving on my dissertation committee and providing professional suggestions on my work.

I thank my collaborators Professor Arjun Deb, Dr. Yijie Wang, and Dr. Tomohiro Yokota for providing the much-needed cardiomyocytes for my projects.

I am also sincerely grateful to all my colleagues from the Optofluidics Systems Lab. I would like to thank Assistant Professor Tingyi "Leo" Liu and Dr. Ximiao "Will" Wen for being my research mentors on micro-fabrication techniques and optical system setup and when I joined the lab. Dr. Yu-Ting "Bill" Chow, Dr. Xiongfeng Zhu, Dr. Tianxing Man, and Pei-Shan "Kylie" Chung have also contributed significantly to my projects with their expertise. Many thanks go to Dr. Kuan-Wen "Dennis" Tung, Yen-Ru Lin, and Hsin Lan for their tremendous support and inspiration.

Finally, deepest thanks to my wife and family for their unconditional love and support throughout all these years.

VITA

Education

2015 – 2018 M.S., Bioengineering

University of California, Los Angeles, USA

2011 – 2014 B.S., Physics with Theoretical Physics

Imperial College London, United Kingdom

Publications and Presentations

[1] Yokota, T., McCourt, J., Ma, F., Ren, S., Li, S., Kim, T., Kurmangaliyev, Y., Nasiri, R., Ahadian, S., Nguyen, T., **Tan, X.**, Zhou, Y., Wu, R., Rodriguez, A., Cohn, W., Wang, Y., Whitelegge, J., Ryazantsev, S., Khademhosseini, A., Teitell, M., Chiou, P., Birk, D., Rowat, A., Crosbie, R., Pellegrini, M., Seldin, M., Lusis, A. and Deb, A., 2020. Type V Collagen in Scar Tissue Regulates the Size of Scar after Heart Injury. Cell, 182(3), pp.545-562.e23.

[2] Kim, T., Vazquez-Hidalgo, E., Abdou, A., **Marvin Tan**, X., Christodoulides, A., Farris, C., Chiou, P., Sloan, E., Katira, P. and Rowat, A., 2020. Beta-Adrenergic Signaling Modulates Cancer Cell Mechanotype through a Rhoa-Rock-Myosin II Axis. Biophysical Journal, 118(3), pp.96a-97a.

[3] Nguyen, A., Trompetto, B., **Tan, X.**, Scott, M., Hu, K., Deeds, E., Butte, M., Chiou, P. and Rowat, A., 2019. Differential Contributions of Actin and Myosin to the Physical Phenotypes and Invasion of Pancreatic Cancer Cells. Cellular and Molecular Bioengineering, 13(1), pp.27-44.

[4] **Tan, X.**, Ngyuen, A., Rowat, A. and Chiou, P., 2018. Large Area Precision Cell Traction Force Measurements Using Gold Disk Mounted Micro-Pillars. 2018 IEEE 12th International Conference on Nano/Molecular Medicine and Engineering (NANOMED).

[5] Xiao, F., Wen, X., **Tan, X.** and Chiou, P., 2018. Plasmonic micropillars for precision cell force measurement across a large field-of-view. Applied Physics Letters, 112(3), p.033701.

[6] Lou, L., Yu, H., **Haw, M.**, Zhang, S. and Gu, Y., 2016. Comparative characterization of bimorph and unimorph AlN piezoelectric micro-machined ultrasonic transducers. 2016 IEEE 29th International Conference on Micro Electro Mechanical Systems (MEMS).

Chapter 1 Introduction

1.1 Overview of Cell Mechanics

The ability to measure the mechanical properties of cells plays an important role in many biological and medical science applications. The study of cell or tissue mechanics is vital to clarifying challenges in physiology [1] and disease development. The mechanical properties of cells impact many characteristics of cell function [2], including mechano-transduction [3] [4], migration [5], and differentiation [6]. They can thus serve as inherent biophysical markers of cell state transitions [7], such as metastasis of cancer cells [8], initiation of leukocytes [9], or advancement through the cell cycle [10]. Furthermore, if a cell misconstrues a mechanical cue or finds itself within an unusual environment, its typical function can be interrupted and disease states can occur [11]. Many human diseases, such as asthma [12], osteoporosis [13], deafness [14], atherosclerosis [15], cancer [16], osteoarthritis [17], glaucoma [18], and muscular dystrophy [19] can be directly triggered by or catalyzed by abnormal cellular or tissue mechanics [11]. Moreover, the mechanical properties of the cytoskeleton are a key factor affecting not only the cell shape, but also of other cellular functions involving spreading, crawling, polarity, and cytokinesis [20] [4] [21] [22] [23]. For example, the deformability of leukocytes is related to the cortical tension produced within a thin actin-rich layer below the plasma membrane, as well as the viscoelastic properties of the cytosol [24] [25]. Additionally, naive mesenchymal stem cells have been shown to exhibit particular phenotypes depending on tissue-level stiffness [26].

Mechanical phenotypes of cancer cells are important for understanding fundamental processes in tumor development [16] and also for developing more effective diagnostics and treatments [27]. A crucial determinant of successful tumor metastasis is the apparent modifications

in the mechanical properties of the tumor cells [26]. It is progressively noticeable in the biophysical communities that cell mechanics is a favorable biomarker for elucidating cell conditions [28]. Traditional structural-based inspection of cell or tissue sample is the benchmark for cancer diagnosis, but this technique necessitates cells to be chemically fixed and thus cancer cell behaviors (e.g., invasiveness, metastatic ability) cannot be evaluated [27]. Detecting cell mechanics is label-free without sample pretreatments [29] and thus can provide new insights into cell behaviors, which is important in various fields, including disease diagnosis and therapy [27], drug screening and assessment [30].

Forces which cells wield on the micro-scale have been discovered as important factors influencing a multiplicity of biological functions, such as cytokinesis [31], migration [32] , vaso-regulation [33], phagocytosis [34], proliferation [6], morphogenesis [4], differentiation [3], activation [35], and motility [36]. In particular, external mechanical forces control cell shape, movement, gene expression, and apoptosis [37], and cells generate protrusive and contractile forces during kinesis, phagocytosis, and cytokinesis [34]. The cytoskeleton and cortical region near the plasma membrane of a cell primarily affects a cell's mechanical properties [38] [39]. It is well-recognized that force can lead to alterations in gene expression, and that forces applied via membrane-based receptors can cause nuclear deformation [40]. External forces transmitted to the cytoskeleton can cause rupture of microtubules, which in turn can initiate a biochemical signaling response [41].

Many human illnesses are associated with unusually strong or weak cellular traction forces, such as cancer malignancy [42], fibrosis [43], hypertension [44], asthma [45], urological disorders [46], muscular dystrophy [47], cardiomyopathy [48]. The highly metastatic A549 cancer cell is

known to exhibit greater traction forces than the non-metastatic BEAS2B cancer cells [8]. Therefore, cell traction forces have the potential as a biomarker for detecting not only circulating tumor cells from human blood, but also for quantifying the metastatic potential of such cells.

Disease-in-a-dish models using induced pluripotent stem cells (iPSC) derived tissues have studied the traction force to understand the underlying causes of disease [49] [50] [51]. Traction forces have also been used to screen the effectiveness or toxicity of drugs related to human diseases [52] [30] [53] [54] [55]. Cellular traction forces can also an important bio-marker for analyzing the quality of human stem-cell derived differentiated cells in the field of regenerative medicine [56] [57]. In the field of heart regeneration, it is imperative that the cell traction forces of iPSC cardiomyocytes be measured and checked for arrythmia in pre-clinical trials, before any human clinical trials be started [58]. These many applications also demand the strong needs of versatile tool technologies for measurements and characterizations of various mechanical properties of biological systems over a wide spatial and temporal scale. In the subsequent sections, we explore several different platforms for the direct measurement of the mechanical material properties of cells.

1.2 Current approaches for cell stiffness measurements

1.2.1 Optical Tweezers (OT)

Optical tweezers employ the gradient forces that act on polarizable materials in the center of a highly focused laser beam [59]. To create adequate gradient force, high numerical apertures are needed, and thus usually either oil or water immersion objectives with numerical apertures (NA) > 1 are employed [60]. In double optical tweezers, two counteracting lasers are concentrated on the same location in 3-dimensions [61]. In such systems, a small numerical aperture is adequate

for stable trapping. Therefore, long working distances up to millimeters can be attained [62]. Optical tweezers must be calibrated by applying techniques such as utilizing the power spectral density of free particle oscillations via the fluctuation dissipation theorem [63] [64], the drag force method using the established viscosity of the medium [65] or Boltzmann distribution methodology where the variation of the average particle position is linked to the trap stiffness of the tweezers [66]. One elegant method of calibration is to directly deduce the force by measuring the asymmetry of the scattered photons to precisely discover the force using the conservation of momentum [67]. This method, however, necessitates utilizing a condenser with a higher NA than the objective.

To implement mechanical measurements, either the laser focus or the sample itself must be shifted. To relocate the laser, piezo controlled reflectors [68] or acoustic optical deflectors (AOD) [69] [70] are frequently used. The response function can be detected by employing either a fluctuating or a step force to intracellular particles such as endogenous vesicles or beads [68] [71]. The bead position is either recorded using video microscopy or position sensitive photo-detectors [72] [73]. The advantage of optical tweezers is that very precise and accurate measurement of cell mechanical properties can be achieved by filtering out noise using lock-in amplifiers [62]. However, the disadvantage is that the measurements are serial in nature and only one particle can be manipulated and imaged at a time, making the measurement throughput extremely low.

1.2.2 Magnetic Tweezers (MT) And Optical Magnetic Twisting Cytometry (OMTC)

Another technique to exert active forces on cells are magnetic tweezers [74] [75]. This is accomplished by either using magnetic gradient forces to exert a force on a paramagnetic particle [75], or applying oscillating magnetic fields to produce mechanical torque on magnetic particles

which are usually fastened to the cell membrane [76]. Magnetic tweezers and OMTC are able to generate forces up to 100 nN [77]. There is also no interaction between the magnetic field and the cell. The system needs a powerful magnetic gradient which can be produced by a multiplicity of coil arrangements [78]. Open cell culture dishes are frequently needed to attain large forces [77], due to the layout of the electric coils generating the magnetic field.

For OMTC, ferromagnetic beads are incubated with the cells and fastened to the exterior either by particular receptors or by general attachment. A transient, powerful magnetic field generates lateral magnetization in the beads [79]. Subsequently, a probe field is operated vertically to the cells, which thus exerts torque on the beads [80]. This vertical field is usually weaker than the lateral magnetization field and can be modified using a sinusoidal or stepped electrical signal. The study of the frequency dependent experimental data uses the same signal processing techniques as for the optical tweezers [81].

For both magnetic methods, the bead movement is usually identified using video microscopy, where a precise control of the force exerted, and a high frame rate are critical [82]. Using single particle tracking software, the positional precision of the bead motion detected can be in the order of several nanometers [83]. Though the study of the response function and the shear modulus for magnetic tweezers is comparable to optical tweezers, OMTC requires a model that links the magnetic torque driven rotational movement to the stiffness of the cell. In this model the attachment area between the cell membrane and the magnetic beads is a critical quantity which is either estimated from literature or is approximated via finite element software [84]. Errors in the attachment area will affect the absolute results, but not the relative comparisons. Magnetic tweezers and OMTC have the benefit that they permit greater forces, and concurrent exertion of

forces on several beads, thus enhancing the potential uses and the throughput of the experiments [85].

1.2.3 Atomic Force Microscopy (AFM)

Atomic Force Microscopy is the most frequently used tool for detecting local cell mechanical properties [86] [1] [87]. A compliant cantilever with a sharp tip mounted at its end is employed to indent the cell or object of concern [88] [89] [90]. AFM is also capable of doing raster scanning of the sample to obtain a topographical map [91]. The deflection of the cantilever is calculated using a laser that is reflected off the surface of the cantilever tip and shines onto photo-detector [92]. AFM has nanometer resolution [93] and can operate in liquid conditions, which makes it particularly suitable for detecting biological samples [94]. To measure the mechanical properties of cells, the cantilever tip is typically spherical [95]. This enables the use of an analysis model such as the Hertz [96] or the Sneddon [97] model which characterizes the force as a function of indentation depth, using the mechanical properties of the substrate. These models are more complicated compared to intracellular particles as the contact area increases while the cantilever indents the cell [98]. With AFM, the microvilli on living mammalian cell surfaces can be imaged [99], nanoscale structures on living bacterial cell surfaces can be revealed at single-molecule level [100], and the dynamic movements of single molecules on cell membranes can be documented by high-speed AFM [101]. To calculate the viscoelastic properties of the cells, a slow methodology can be added to a well-defined fluctuation. Using lock-in amplifiers this was shown to access the localized frequency dependent viscoelastic properties of living cells [102] [103]. Major benefits of the AFM are the wide range of available forces, mature commercial microscopes, and a multitude of cantilever geometries [104]. Apart from topography imaging, AFM also

presents high-resolution images of cellular mechanical properties, hence functioning as a reliable tool for contrasting mechanics with the shapes and roles of the sub-cellular organelles [105]. Conversely, AFM measurements usually investigate the cellular exterior and not intracellular properties [106]. It is conceivable to deduce bulk properties with substantial indentation distances, but analysis is more challenging. Furthermore, as cell chambers are open to permit cantilever entry, specific attention for the proper environments of the cells such as pH, temperature and osmolarity need to be ensured [107]. The use of AFM in sensing cell mechanics in the past years have spawned significant developments in understanding cell phenotypes [108], contributing substantially to the field of cell biology and medicine [42]. One disadvantage of AFM is the low throughput as only one cantilever can operate on one sub-cellular region at a time, and therefore cannot achieve parallel measurements. Detection of the active vertical traction forces of cardiomyocytes has been reported. Cardiomyocytes obtained from subjects with dilated cardiomyopathy exhibited decreased active vertical traction forces [109]. However, AFM is not able to detect horizontal traction forces which cells exert. Therefore, there are no scientific literature reporting the use of AFM to measure lateral cell traction forces.

1.3 Current Approaches For Cell Traction Force Measurements

1.3.1 Monolayer Tissue On Cantilevers

Coordinated responses of a group of cells can be studied by growing a continuous monolayer of muscle cells as a monolayer on a mechanical cantilever [110], in which the averaged force output of a group of cells can be read out from the curvature of the cantilever. In one such example, a polymer-based cantilever is patterned with microgrooves so that the cardiomyocytes can align to the cantilever in order to make a higher cantilever deflection in response to contraction force of cardiomyocytes [111]. Another example is a variable-modulus sheet of vascular muscle

cells grown on a cantilever substrate that measures vascular tissue functional contractility on substrates with a range of pathological and physiological moduli [112]. The limitation of this method is the lack of mechanical interactions' information between cells, subtypes of cells, potential synergistic, or antagonistic force generating activities.

1.3.2 Conventional Cell Traction Force Platforms

Elastic micro-pillars utilize isolated mechanical pillar structures to simplify the process of extracting traction forces. By treating a single elastic micro-pillar as a cantilever beam, Hooke's law can be used to convert the displacement of the pillar tip to the traction force exerted by the cell [113]. Hooke's law simply implies that the traction force exerted at the tip of the micro-pillar, is directly proportional to the displacement at the pillar tip. The constant of proportionality is the spring constant of the micro-pillar, which can be easily calculated from the young's modulus of the material and the geometry of the pillar using solid mechanics theory [114].

Waveguide-type micropillars require light illumination from the bottom of a PDMS substrate [115]. The PDMS pillars function as waveguides because they have a higher refractive index than the surrounding cell media. This allows the pillars to look brighter than the cell media under the microscope. However, the background noise is high due to the transmission of light through the transparent PDMS substrate [115]. This leads to a low signal-to-noise ratio. Moreover, the waveguide pillars suffer from the leakage of light from the sidewalls of the pillars, when the pillar displacement is large. This is because at large pillar displacements, the incident angle of light inside the waveguide becomes smaller than the critical angle. This causes the bright spots to look elongated under microscopy [116]. Both factors cause measurement errors and compromise the accuracy of pillar position estimation under low magnification imaging.

As for fluorescent fibronectin coated pillars, the nature of contact printing makes it difficult for the pillars to have a uniform coating of fluorescent fibronectin [117]. Thus, the fluorescent images of the pillar tips do not fit the shape of the gaussian function. Moreover, the brightness of fluorescence degrades over time, reducing the signal-to-noise ratio and hence the measurement precision [118]. Consequently, high magnification lenses have to be used to improve the precision of the pillars' positions.

Fluorescent beads embedded in continuous polymer gels have also been used for conventional cell traction stress microscopy. Through tracking nanoparticles embedded in an elastic film, traction force distribution can be extracted through reverse engineering [119]. This type of substrate has the advantage of allowing the growth of cell monolayers, because the substrate is flat.

All the cell traction force microscopy methods mentioned above require the use of high numerical aperture (N.A.) optics to accurately determine the tracer particle locations needed for extracting the forces, and thus are inherently limited to measuring small numbers of cells. Through mathematical curve fitting algorithms, sub-pixel position accuracy can be achieved [115]. One method for determining the positions of the fluorescent tracers is to fit a 2-dimensional gaussian function to the intensity profile of the fluorescent tracer [120] [121]. In order to achieve sufficient precision of the gaussian fit, a sufficient number of pixels are required. The precision of the gaussian fit also depends on the signal-to-noise ratio of the fluorescent signals. The larger the signal-to-noise ratio, the less the number of pixels is required to achieve the same sub-pixel precision of the gaussian fit. However, the signal-to-noise ratio of the fluorescent tracers is not sufficiently high enough to use low N.A. and low magnification (20x) objective lenses for sufficiently precise gaussian fitting for sub-cellular resolutions. Therefore, high N.A. optics

corresponding to high magnifications (> 40x) are required. The small field-of-view (FOV) of high N.A. optics (< 0.018mm^2) preserves the spatial resolution of traction force analysis. This however, limits the measurement area to a small number of cells.

Attempts to use 10x magnification to achieve fields-of-view of approximately 0.56mm^2 have resulted in the severe reduction of sub-cellular spatial resolution [122] [123] [124] [125]. It is interesting to note that in the literature which use 10x magnification [123] [124], there is significant overlap in the interquartile range of traction force data between the control and experimental groups, such that thousands of cells are required to prove statistical significance. However, in the literature which use 40x magnification [8] [126] [42], only about 20 cells were needed to prove the statistical difference between the control and experimental groups. Despite using 10x magnification, these conventional TFM techniques are still unable to reach a field-of-view into the order of centimeters squared, which is the length scale of tissues in human organs.

1.3.3 Fluorescently Labelled Elastomeric Contractible Surfaces (FLECS)

FLECS is an approach for high throughput single cell mechanics measurement [127]. However, its need of seeding isolated cells on tracer structures limits its application for quantifying mechanical responses from interconnected tissues. The authors acknowledged that the differences in traction stress distributions between osteocytes and adipocytes (obtained from hundreds of thousands of cells) were less apparent than by using micro-post arrays with only a sample of 13 to 62 cells [128]. The authors additionally recognized that conventional cell traction force microscopy methods should remain the standard for addressing specific biological questions relating to sub-cellular force generation by small numbers of cells.

1.4 Motivation for Large Area Concurrent Measurements

The limitations of the abovementioned technologies present a challenge for studying multicellular mechanical interactions and coordination, that often involve tens of thousands of cells in a tissue form. Although existing high N.A. and large field of view technologies combining multiphoton imaging have been demonstrated for high resolution imaging for monitoring neural activities [129], the digital optical excitation and its serial scanning nature of these methods do not offer needed spatial and temporal resolution for quantifying biomechanical responses involving fast interactions between cells [130].

In the medical field of heart regeneration, cardiomyocytes in the body reside within interconnected syncytial tissue [131]. Thus, there is a need to measure changes in the traction force across large numbers of cardiomyocytes over a large area, while maintaining sub-cellular resolution. In the field of cardiac drug discovery, sub-cellular resolution assays of contraction and relaxation of not just single myocytes but a large area syncytium of myocytes [132] would be a significant step forward as it would enable the testing of the effect of various genetic [133] [134] and environmental [135] perturbations on the physiological function of myocytes. Attempts have been made to measure the mechanical displacement [136], mechanical movement [137], and mechanical strain [138] of cardiomyocytes over large fields-of-view exceeding. However, these methods not only suffer from poor spatial resolution, but they are also not able to extract the quantitative traction stresses or forces.

In order to quantify the effect that the behavior of distant cells within cardiomyocyte tissue have on each other, the measurement field-of-view must span over distances of millimeters. Engineered cardiac tissue spanning 0.5 mm x 0.2 mm have been studied [139], while the heart of a mouse spans 10 mm x 4.2 mm [140]. A platform for measuring how the traction force of cells a

distance of millimeters apart affect each other, would be valuable for pre-clinical trials in relation to testing drugs or for testing the quality of stem cell derived cells for tissue regeneration. Such a platform would also be important for studying the long range communication of cells in disease-in-a-dish models. However, existing traction stress measurement platforms discussed above are not only limited to fields-of-view of 0.56mm², but also suffer from poor sub-cellular resolution when operated at 10x magnification. Consequently, their limited field-of-view does not permit the tracking of dynamic changes in the traction stress as a single cardiac beat propagates across a large cardiac tissue area, within the time-scale of milliseconds. Therefore, it is critical to have new traction force measurement tools with a field-of-view as large as possible without compromising the spatial resolution. In the following chapters, we present three different traction force measurement tools that offer larger fields-of-view concurrent measurements over compared to the prior technologies discussed above.

Chapter 2 Gold Disks Micro-Pillar Platform

2.1 Introduction

This chapter is to introduce a new gold disk micro-pillar (GDMP) platform that can provide continuous imaging over an area of 0.60mm^2 with a measurement precision of 75 nm using a 10× magnification objective lens. On this platform, gold micro-mirrors were mounted to the tips of the PDMS pillars as shown in Fig. 2.1. Because gold is highly reflective, light is scattered by the circular edge of the micro-mirror. The symmetric ring of the micro-mirror provides a gaussian image under dark field microscopy. The strong scattering signals allow to clearly image the micro-mirrors with a 10x objective lens that can greatly increases the measurement field of view over prior platforms which require at least 40x magnification. The strong scattering signals also reduce the exposure time needed for collecting enough photons during the measurement of rapidly changing dynamic behaviors.

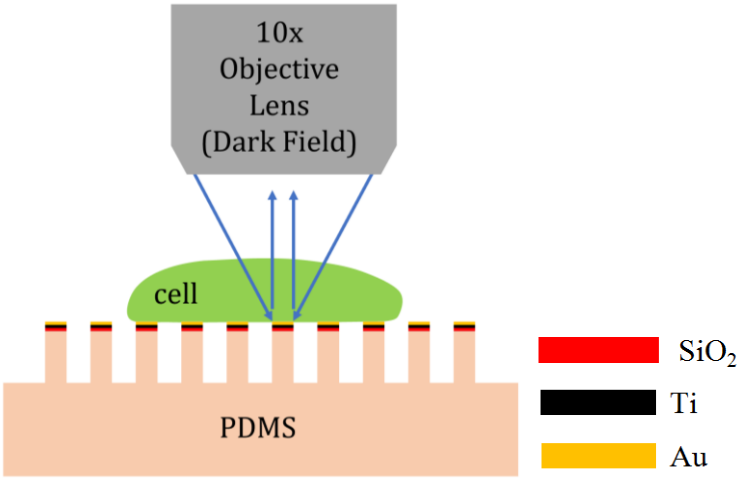

Fig. 2.1. Schematics of a GDMP platform. The tips of PDMS micropillars are imaged under dark field microscopy. scatter light by the circular edge of gold micro-mirrors. The symmetric and

circular rings of the gold disks mounted on pillars provide strong scattering signals for imaging under a low N.A. optics setup.

2.2 Methods

2.2.1 Fabrication

The method of fabrication was modified from that of Xiao, Fan *et al* [141]. Firstly, a silicon wafer was thermally oxidized to produce thermal oxide layers as shown in Fig. 2.2(a). The photoresist AZ5214E was patterned on top of the top oxide layer as shown in Fig. 2.2(b). The photoresist was used as an etching mask to etch the top oxide layer. The top oxide layer was etched using reactive ion etching (RIE) to produce the oxide hard mask as shown in Fig. 2.2(c). This oxide layer was used as a hard etching mask to perform deep reactive ion etching (DRIE) on the silicon material. The oxide layers were then removed by selective wet etching using hydrofluoric acid to produce the silicon mold shown in Fig. 2.2(d). Deposition of silane was done on the silicon mold by placing both the silicon mold and liquid silane in the same chamber. The chamber was vacuumed and then left sealed overnight. The reduced pressure in the chamber caused the silane to vaporize. This allowed the silane vapor to deposit onto the silicon mold. Uncured PDMS (Sylgard 184) was then poured onto the silane treated silicon mold. The uncured PDMS was placed in a chamber and vacuumed to remove the air bubbles. The PDMS was cured in an oven at 60°C overnight to form the PDMS mold shown in Fig. 2.2(e). Thereafter, the PDMS mold was separated from the silicon mold.

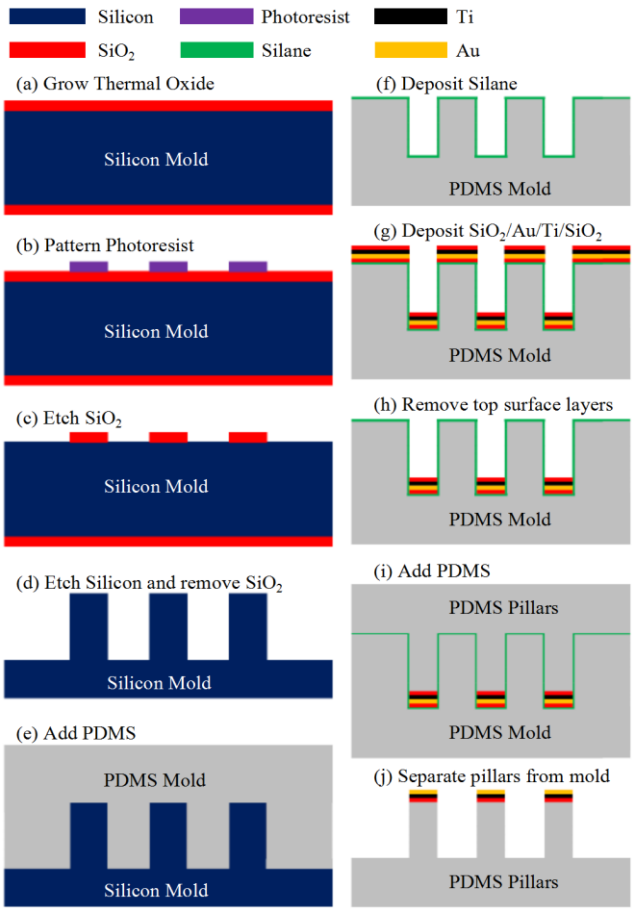

Fig. 2.2. Fabrication process flow for the gold disk micro-pillars (GDMP) platform. Starting from a thermally oxidized wafer (a), the oxide hard mask was patterned (b) and etched (c). The silicon mold (d) is used to make a PDMS mold (e). The PDMS mold was treated with silane (f) before having a multi-stack layer of SiO_2/Au/Ti/SiO_2 deposited into it (g). Polyimide tape was used to remove the top surface layers (h). PDMS was then added (i) before separating the pillars from the mold (j) to get the final device.

As shown in Fig. 2.2(f), silane was deposited onto the PDMS mold as per the method described above. A multi-stack layer of SiO_2/Au/Ti/SiO_2 was then deposited via electron beam evaporation, onto the silane treated PDMS mold, as shown in Fig. 2.2(g). The multi-stack layers

at the top surface of the PDMS mold were removed using polyimide tape, to leave the layers only inside the wells as shown in Fig. 2.2(h). Uncured PDMS mixed with platinum catalyst was poured into the PDMS mold as shown in Fig. 2.2(i). After vacuuming out the air bubbles, the PDMS was left to cure at room temperature. The SiO_2 layer automatically adheres to the PDMS pillar layer during the curing process. After 6 hours, the PDMS was cured by the platinum catalyst.

The entire device was then submerged in methanol. A tweezer was pushed in between the PDMS pillar layer and the PDMS mold layer to separate the two layers. Due to the poor adhesion between SiO_2 and Au, the two layers separated easily when the pillars were removed from mold. This resulted in the Au/Ti/SiO_2 stack layer being attached to the tip of the PDMS pillars as shown in Fig. 2.2(j). The PDMS pillars were then exposed to ultrasound while still being immersed in methanol, in order to shake those pillars which have fallen down. This helped to ensure that the pillars stood upright.

The PDMS pillars were then dried in a super-critical point dryer (Tousimis 915B). The pillars were treated with oxygen plasma to introduce hydroxyl groups onto the PDMS surface. The pillars were then immersed into Pluronic F127 in order to passivate the PDMS sidewalls. The pillars were then immersed in 2-mercaptoethanol to form an adhesion layer between the gold and fibronectin protein. Finally, the pillars were immersed in fibronectin to facilitate cell adhesion to the gold disks.

2.2.2 Cell seeding

We used both Henrietta Lacks cervical cancer (HeLa) cells and pancreatic ductal adenocarcinoma (PANC-1) cells to test our micro-pillar platform. The cells were suspended in Dulbecco's Modified Eagle's medium (DMEM) in a petri dish. The glass slide containing the gold

disk micro-pillars was immersed into the cell media containing the cells, inside the petri dish. The entire petri dish was then placed into an incubator at 37℃ for 20 hours. This allowed the cells to fall downwards in the DMEM and thus to adhere to the fibronectin coated pillars. The cell membrane forms focal adhesions by binding their integrins to fibronectin. This allows the cell membrane to adhere to the fibronectin-coated pillars. The cells were then stained for fluorescence using Wheat Germ Agglutinin (WGA), Alexa Fluor 488 conjugate. The cells were then observed under a microscope.

2.3 Results

Under 10× magnification, the field-of-view of 894μm × 670μm is obtained as shown in Fig. 2.3. Under 20× magnification, the field-of-view is 447μm × 335μm, as shown in Fig. 2.4. With the strong scattering signals induced by single gold disks on top of the pillars, the difference between the intensities of the gold disks and the background is large, which gives a high signal-to-noise ratio that can increase the curve fitting accuracy for determining the pillar location.

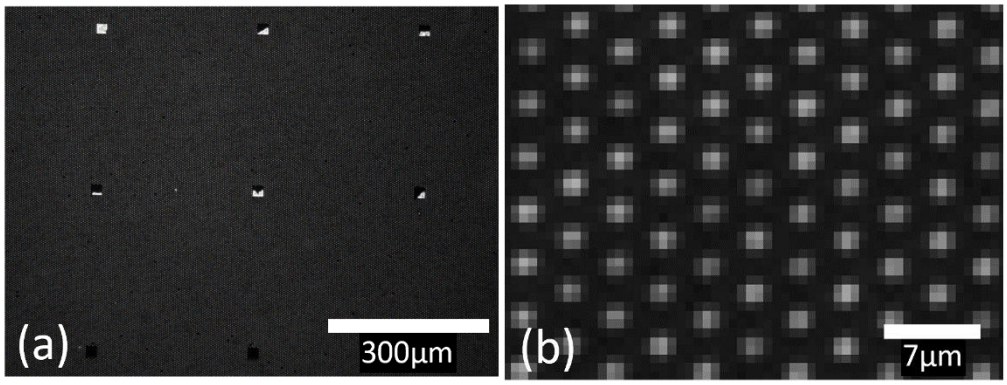

Fig. 2.3. (a) The entire view of the gold disk array seen under dark field imaging using a 10× magnification objective lens. (b) A digitally zoomed-in image showing the gold disks.

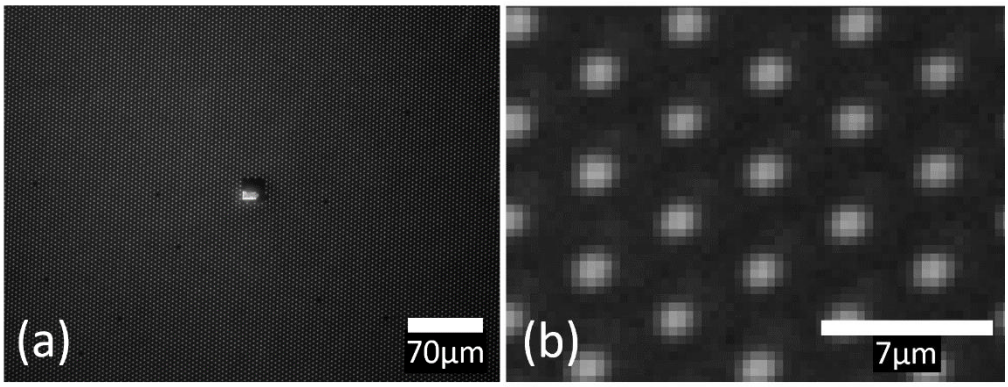

Fig. 2.4. (a) The entire view of the gold disk array seen under dark field imaging using a 20× magnification objective lens. (b) A digitally zoomed-in image showing the gold disks.

To quantify the measurement precision of the pillar positions on the GDMP platform, we used the same method as F. Xiao *et al* [141] by super positioning two images of the same group of pillars, one image as a reference and the other image from a rotated chip, to extract the measurement error from our optical system. The positions of these gold disks were determined via gaussian fitting, and their positions from both images were aligned. Due to systematic errors present in the imaging acquisition process, the locations of the bright spots from both images will have a finite misalignment. The difference of the pillar positions was taken as the measurement error. Under 10× magnification, the median error was 75nm (Fig. 2.5(a)). Under 20× magnification, the median error was 27nm (Fig. 2.5(b)).

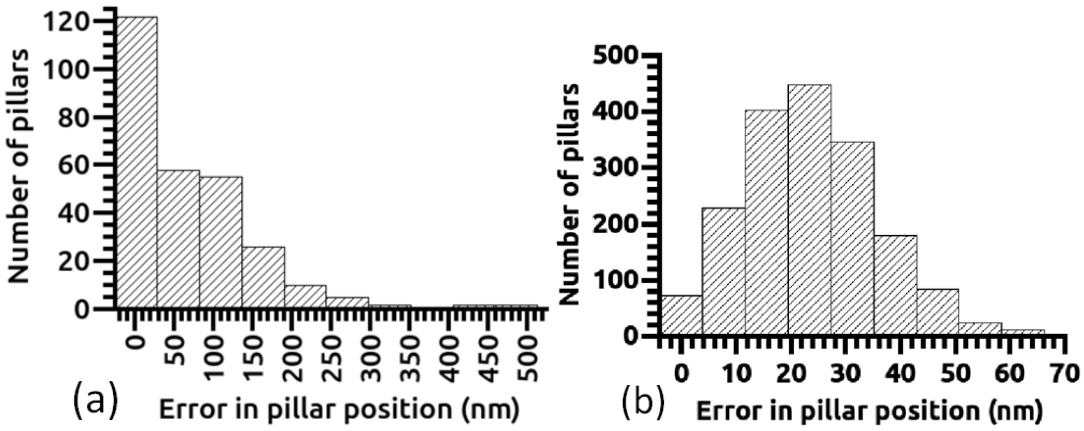

Fig. 2.5. Histograms showing the errors in the position of the pillars. (a) Errors obtained under 10× magnification. (b) Errors obtained under 20× magnification.

In order to convert the displacement of the pillar tips into the traction force, we used the equation for a long cylindrical-shaped micropillar from F. Xiao *et al* [141]. The micropillar has a diameter of 1.7μm, a height of 5.8μm, and a Young's modulus of 2.0MPa. We measured the Young's modulus of the bulk PDMS using the uniaxial compression test according to Wang *et al* [142]. The height of the pillars depends on the thickness of the Au/Ti/SiO_2 stack and the depth of the silicon mold. The depth of the silicon mold was measured using a Scanning Electron Microscope (SEM).

In order to demonstrate that GDMP is able to measure cell traction forces, we seeded Henrietta Lacks (HeLa) cells and pancreatic ductal adenocarcinoma (PANC-1) cells on the platform and imaged them under dark field microscopy. The area shown in Fig. 2.6(a) spans 670μm × 670μm, which measures the traction forces of hundreds of cells within a single image, using a 10× objective lens. We found that HeLa cells mainly exert radially inward traction forces from the circumferences of the cells, as shown in Fig. 2.6(b). The directions of the arrows depict the direction of the force exerted by the cell on the pillar, while the arrow's length is proportional

to the magnitude of the traction force. The color of the vector arrows also represents the magnitude of the traction forces. Cell traction forces of pancreatic ductal adenocarcinoma (PANC-1) cells measured under a 20× objective lens are also shown in Fig. 2.7. We observed that the PANC-1 cells mainly exert radially outward forces.

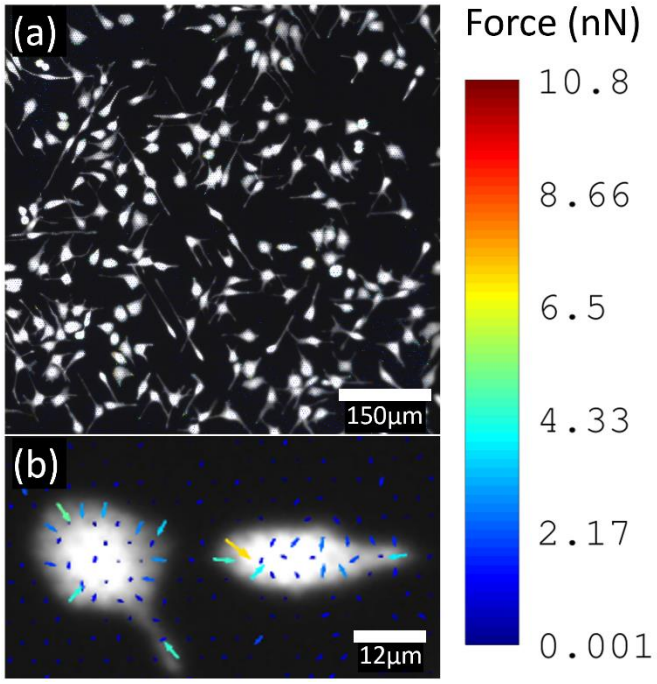

Fig. 2.6. (a) Colored vector arrows representing the traction forces of HeLa cells, superimposed on the 10× magnification fluorescent image of the cells. (b) Zoomed-in image showing individual cells.

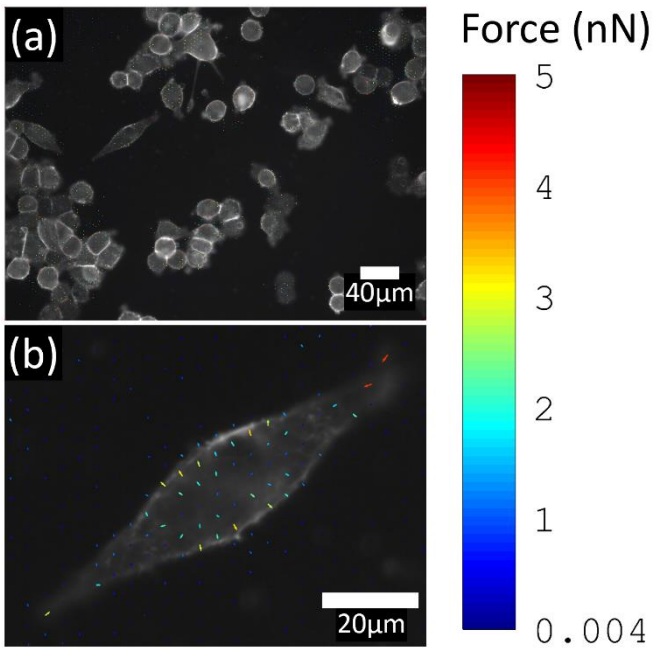

Fig. 2.7. (a) Colored vector arrows representing the traction forces of PANC-1 cells, superimposed on the 20× magnification fluorescent image of the cells. (b) Zoomed-in image showing an individual cell.

2.4 Conclusion

We have shown that by fixing gold disks on top of PDMS micro-pillar tips, the positions of the pillars can be measured down to a measurement precision of 75nm even when using a low magnification 10× objective lens for imaging. This is because the gold disks provide a high signal-to-noise ratio for precise gaussian fitting. We have proven that our platform is able to measure cellular traction forces over a large area under 10× magnification without sacrificing the sub-cellular precision of the pillar displacements. A maximum field-of-view achieved by the GDMP approach was 0.60 mm^2. This platform permits the study of cell mechanics by gathering data from a large number of cells within a single image. However, this platform does not support the growth or maintenance of continuous cell sheets, as there are gaps between the micro-pillars which adherent cells do not like. The gaps between the micro-pillars make it difficult for adherent cells to connect with each other. In the next chapter, we demonstrate an improved platform which combines the high signal-to-noise ratio of gold and the ability to support continuous cell and tissue sheets.

Chapter 3 Gold nanoparticles embedded in PDMS

3.1 Introduction

This chapter is to introduce a new traction force measurement platform with gold nanoparticles embedded near the surface of a continuous PDMS film. Under dark field imaging, the strong scattering signals of these 400nm gold nanoparticles allow us to precisely locate their positions under a low magnification 20× objective lens. A new Fourier transform assisted machine learning approach is utilized to extract the traction force distribution applied on the film based on the coupled gold nanoparticle displacements. With this platform, we can measure the traction stress distribution produced by a continuous cell sheet of neonatal rat ventricular cardiomyocytes (NRVMs) beating over an area of 0.15mm^2 with sub-cellular resolution using a 20× objective lens.

3.2 Methods

3.2.1 Fabrication

The bio-sensor devices were fabricated by first spin coating a layer of photoresist (AZ 4620, 2500rpm, 60s) onto a glass slide, and baking it at 90 Celsius for 3 minutes. Then, gold nanoparticles of diameter 400nm suspended in citrate buffer (Sigma-Alrich 742090) were randomly deposited onto the photoresist and left to dry in a vacuum desiccator (Thermo Scientific™ 53100250) overnight, as illustrated in Figure 3.1(a). A mixture of polydimethylsiloxane (PDMS) comprising 1 part of Sylgard 184 (Dow Corning) with 6 parts of Sylgard 527 (Dow Corning) was then poured onto the surface of dried gold nanoparticles. The Sylgard mixture was put under vacuum (500mTorr) to remove the air bubbles before a coverslip glass was put on top of it, as shown in Figure 3.1(b). The devices were then left to cure in the oven

at 60 Celsius for 12 hours. Thereafter, the devices were released by immersing them into acetone overnight to dissolve the photoresist. This reveals the final structure shown in Figure 3.1(c).

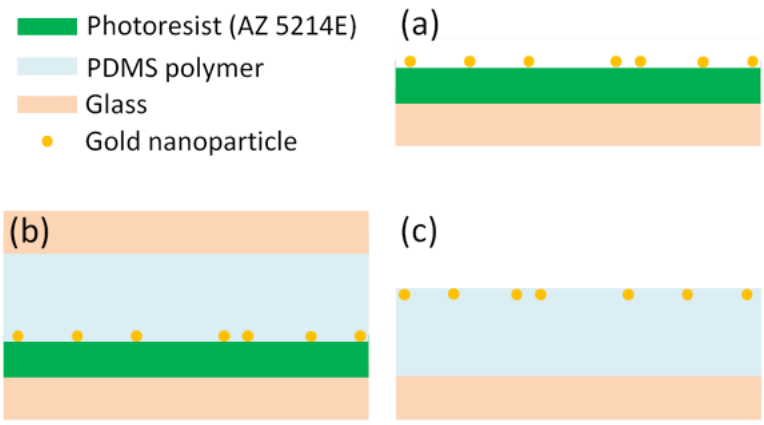

Fig. 3.1. Fabrication of gold nanoparticles in PDMS. (a) Photoresist was spin coated and baked on glass. Then gold nanoparticles suspended in water were deposited and dried overnight. (b) Uncured PDMS polymer was poured over the gold nanoparticles and capped with a glass coverslip, then left to cure overnight. (c) Photoresist was dissolved by immersion in acetone overnight to release the final device.

3.2.2 Cell seeding

Matrigel (at concentration of 83µg/mL) was then coated for 12 hours on the surface of the PDMS device. On day 1, neonatal rat ventricular cardiomyocytes (NRVMs) were seeded on the device. On day 3, the cells were stained with Calcein AM (Invitrogen™), before they were imaged under dark field and fluorescence microscopy (Zeiss AxioScope A1, EC Epiplan-Neofluar, 20×, N.A. = 0.5), as shown in Figure 3.2(a).

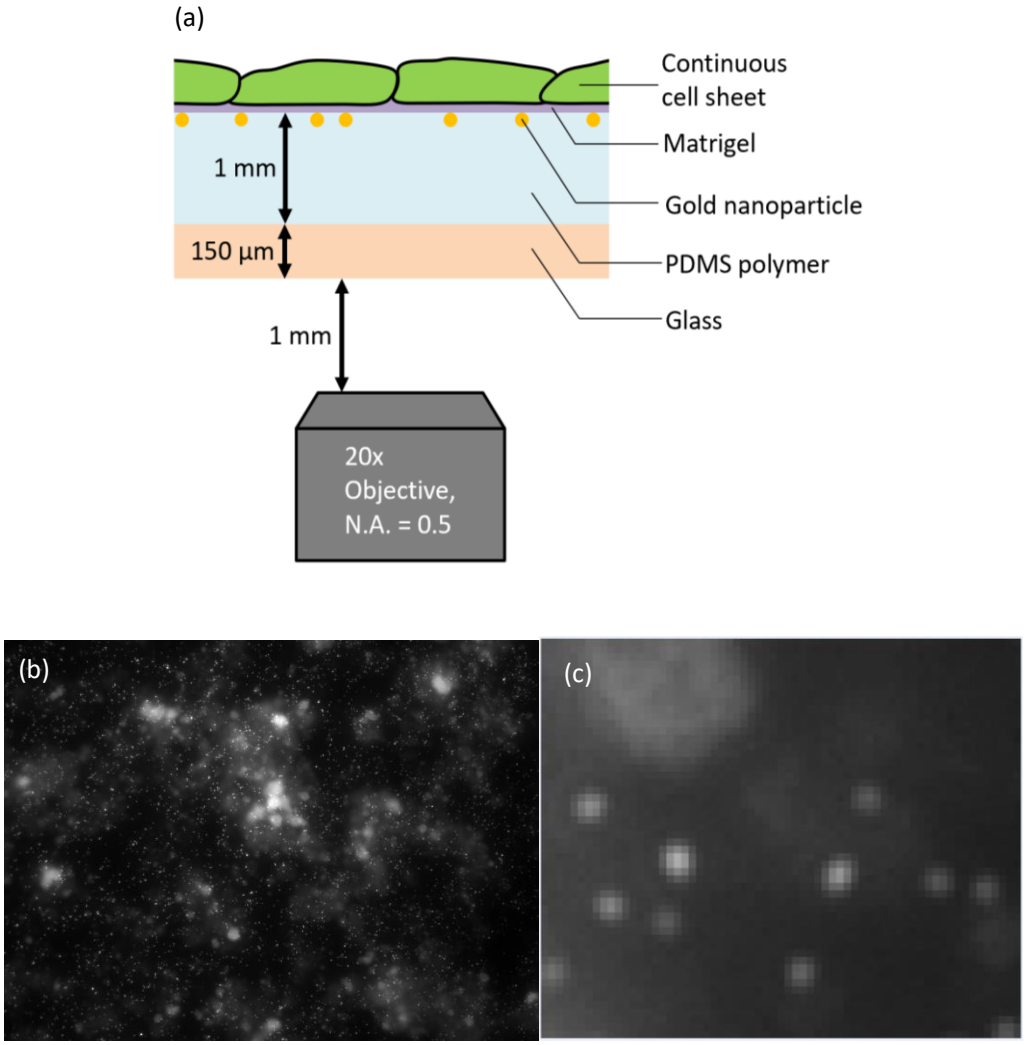

Fig. 3.2. (a) Schematic showing the experimental setup. (b) A dark field image frame spanning 447µm × 335µm, taken by a 20x objective lens. (c) A zoom-in area spanning 21µm by 17µm.

The gold nanoparticles were also imaged under dark field microscopy, as shown in Figures 3.2.2 (b)(c). The gold nanoparticles moved when the cells were beating, due to the mechanical coupling between the cells and the substrate. The displacement of the gold nanoparticles was obtained from the dark field images through the gaussian fitting method used by F. Xiao *et al* [141].

3.2.3 A machine learning approach to extract traction forces distribution

Before the images obtained from microscopy could be processed, the numerical model needed to be built. The numerical model was built by first generating 2000 different scenarios of random continuous stress distributions in COMSOL Multiphysics (finite element software) by using 2-dimensional random functions. Random stress distributions were generated from a 2-dimensional Fourier series, using random numbers for the amplitude and phase terms, according to equation 1.

$$Stress(x,y) = \sum_{-n}^{n}\sum_{-m}^{m} A_{m,n}\cos[w(mx+ny)+\phi] \qquad (eqn\ 1)$$

$$\text{where} \quad w = \frac{2\pi}{\lambda} = 2\pi f$$

$$\lambda = 1\ \text{mm}$$

$$A_{m,n}\ and\ \phi\ \text{are random numbers}$$

An example of the stress distribution is shown in Figure 3.3(a). The stress distributions were applied as boundary loads on the top surface of the PDMS device in COMSOL.

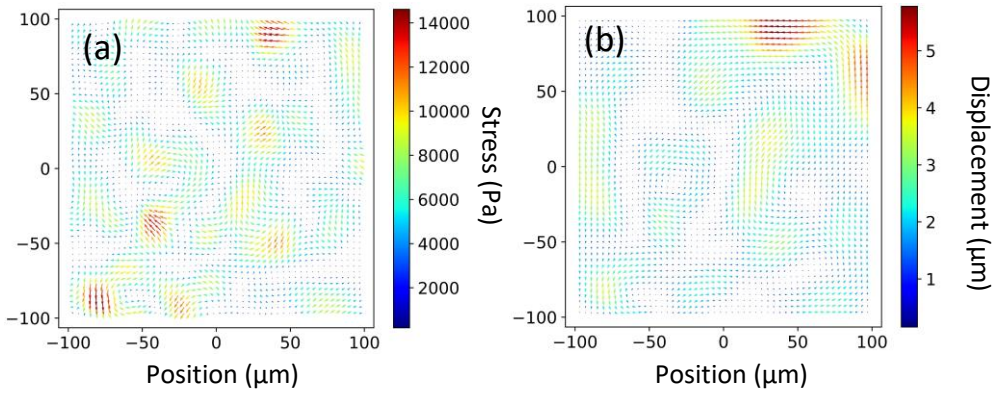

Fig. 3.3. Examples of training data used for machine learning. (a) Randomly generated stress distribution. (b) Corresponding displacement fields solved by COMSOL software.

A total of 2000 different random stress distributions were imported into the COMSOL mechanics simulation. Stationary studies were done in COMSOL to solve for the equilibrium displacement of the PDMS surface. One example of the displacement of the PDMS surface is shown in Figure 3.3(b). Thereafter, 2000 different scenarios of stresses and displacements were used to train the linear regression machine learning model (scikit-learn).

3.3 Results

Under 20× magnification, the field-of-view is 447μm × 335μm, as shown in Fig. 3.2(b). To reduce computational time, an area spanning 200μm × 200μm was selected from the video taken by the microscope. Two image frames were used to calculate the displacement of the gold nanoparticles. The reference frame was chosen as the frame in which the cells were not beating. The peak frame was chosen as the frame in which the cells and gold nanoparticles had the largest displacement. The displacement was taken to be the difference in the positions of the gold nanoparticles between the peak frame and the reference frame.

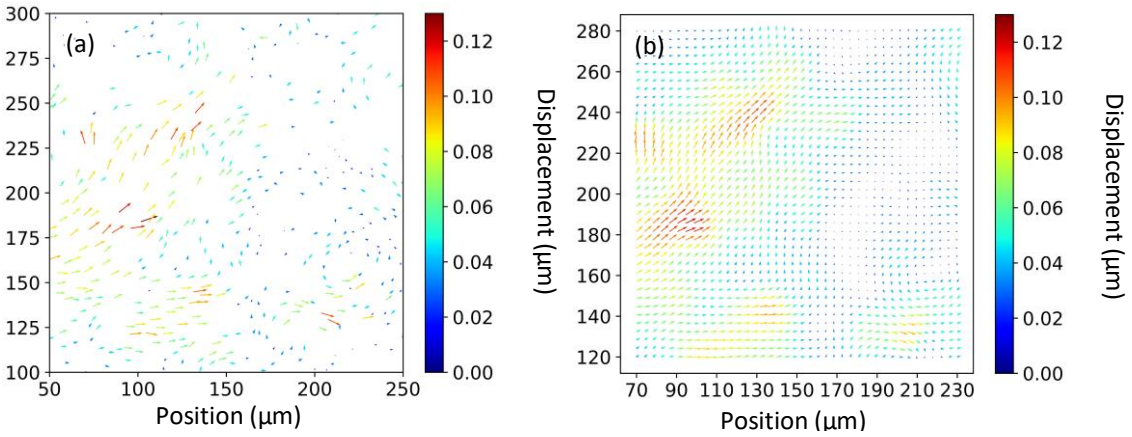

Fig. 3.4. (a) Experimentally extracted displacements of the gold nanoparticles. (b) Interpolated displacements.

Fig. 3.4(a) shows the displacement of each of the gold nanoparticles. The displacements in Fig. 3.4(a) were then interpolated and a two-dimensional Fourier transform filter was applied to process the interpolated data to eliminate the noisy components at high spatial frequencies. The resulting interpolated displacements after Fourier filtering are shown in Fig. 3.4(b). The displacements from Fig. 3.4(b) were then input into the machine learning model. The machine learning model then outputted the stress distributions as shown in Fig. 3.5(a). The predicted stress distributions were then inputted back to the COMSOL software to find the corresponding simulated displacements in Fig. 3.5(b). These simulated displacements were compared with the experimentally obtained and interpolated displacements (Fig. 3.4(b)) to find the fractional error using the expression:

$$\frac{\delta u}{u} = \sqrt{\frac{\sum_{x,y}(u_s(x,y)-u_a(x,y))^2+\sum_{x,y}(v_s(x,y)-v_a(x,y))^2}{\sum_{x,y}(u_a(x,y))^2+\sum_{x,y}(v_a(x,y))^2}} \qquad (eqn\ 3.3.1)$$

where $u_s(x, y)$ and $v_s(x, y)$ are the x and y vector components of the simulated displacement from COMSOL in Figure 3.5(b), while $u_a(x, y)$ and $v_a(x, y)$ are the x and y vector components of the interpolated displacement in Fig. 3.4(b). Note that the displacements are functions over space (x,y). A prediction error of 14% is obtained by our current approach.

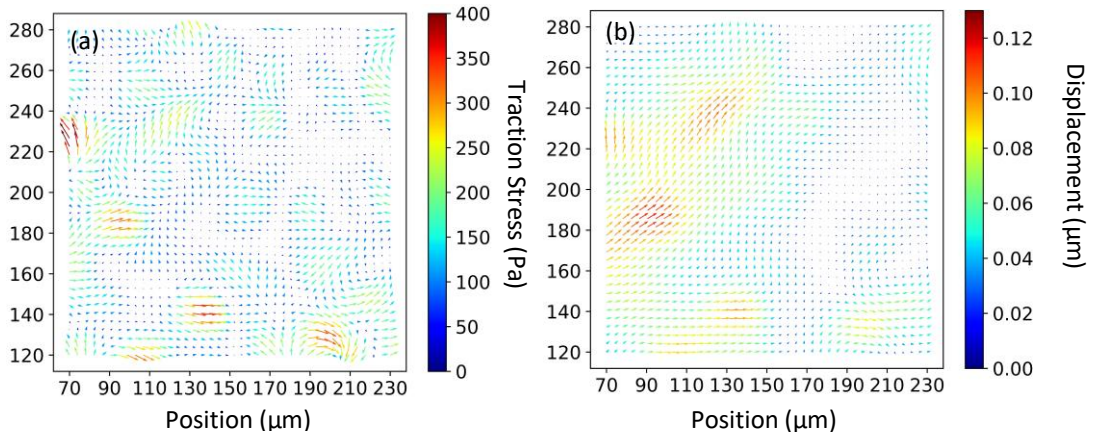

Fig. 3.5. (a) Stresses predicted by the machine learning model. (b) Simulated displacements from COMSOL software after using the predicted stresses as the boundary load.

3.4 Conclusion

We have demonstrated a new machine learning assisted large area traction force measurement platform. By utilizing the physical simulation and machine learning models, we can extract the vector force distribution with an error of 14%. While this platform is able to support quantitative measurement of a continuous cell sheet at either 20x or 10x magnification, the maximum possible field-of-view is still limited to 0.60 mm^2, which is insufficient for studying the

long range communication of cells in a tissue sheet. In the next chapter, we explore a platform capable of expanding the field-of-view to 4.8 mm by 2.7 mm.

Chapter 4 Diffractive Optical Tracers (DOTS)

4.1 Introduction

Here, we present our Diffractive Optical Tracers (DOTS) platform utilizing the colors of digital pixels of an image sensor to enable real-time measurement of dynamic traction forces over a large field-of-view (4.8 mm by 2.7 mm) with a sub-cellular spatial resolution. This platform consists of an array of diffraction grating disks bonded onto a PDMS surface. When cells exert traction forces on the substrate, these disks tilt and reflect different colors of light into the camera lens.

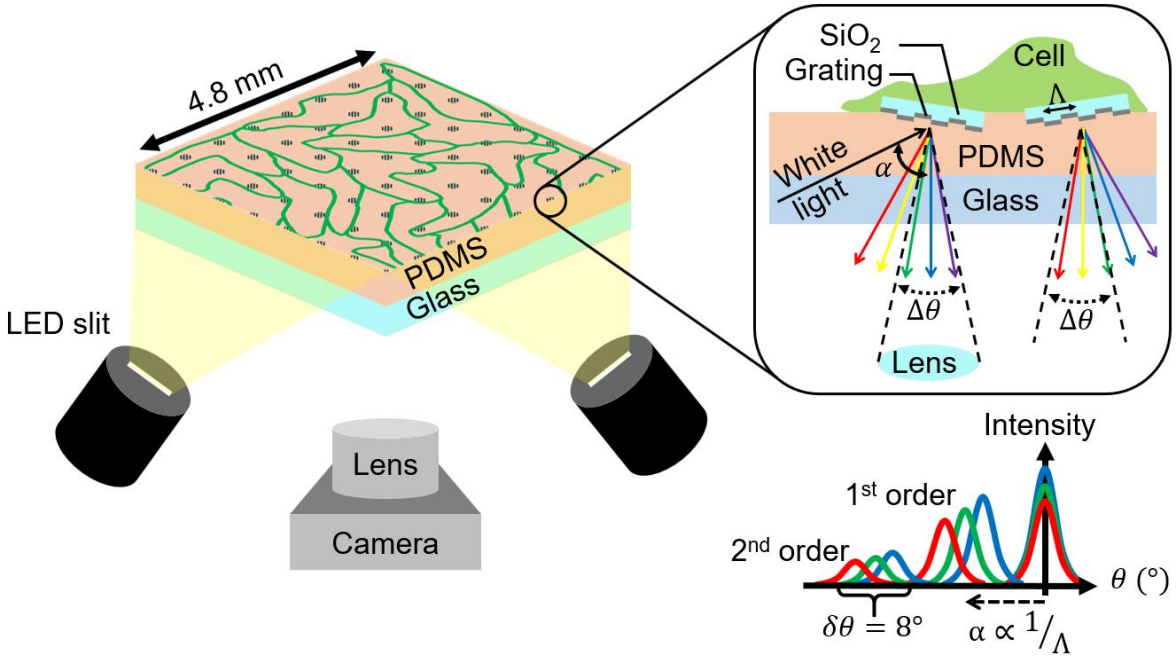

Fig. 4.1. Device operation and principle of DOTS

The relationship between the colors of light reflected by mirrors and the corresponding tilting angles can be calibrated. This dynamic tilting angle information can in turn allow us to reconstruct dynamic traction force distribution exerted by the sheet of cells on the surface. The camera lens was set at an angle (α) to collect the 2nd order diffraction dispersion caused by these

grating mirrors. A small numerical aperture (N.A.) camera lens was used to ensure only light rays within a small angle range ($\Delta\theta$) from each mirror will be collected for imaging. The angle by which the 1st and 2nd order diffraction maxima are directed, is approximately inversely proportional to the periodicity of the diffraction grating. We choose to use the 2nd order diffraction maxima because it can detect a wider range of tilting angles over a larger area for the same change in color, as compared to the 1st order. The 2nd order provides a wider range of tilting angles while the 1st order provides higher sensitivity. To achieve 2-dimensional measurement of the tilting angles & hence traction stress, the 2 LED slits are placed perpendicularly to each other, and switched alternately on and off using an electronic circuit.

We seeded neonatal rat ventricular myocytes (NRVMs) on the DOTS device. The myocytes beat spontaneously and exert dynamic traction stresses on the surface of the device. This caused the grating disks to tilt, thereby producing color changes as seen from the camera. Here we show the entire field of view imaged by the camera. We selected one video frame with the x-direction light source switched on (Fig. 4.2), and show the different colors resulting from the different tilting angles of grating disks. As seen in the left inset of Fig. 4.2, the disks appear with different colors due to having different tilting angles. The red disk in the right inset of Fig. 4.2 corresponds to a tilting angle of -4 degrees, the center disk is at 0 degrees, and the right cyan-colored disk corresponds to +4 degrees.

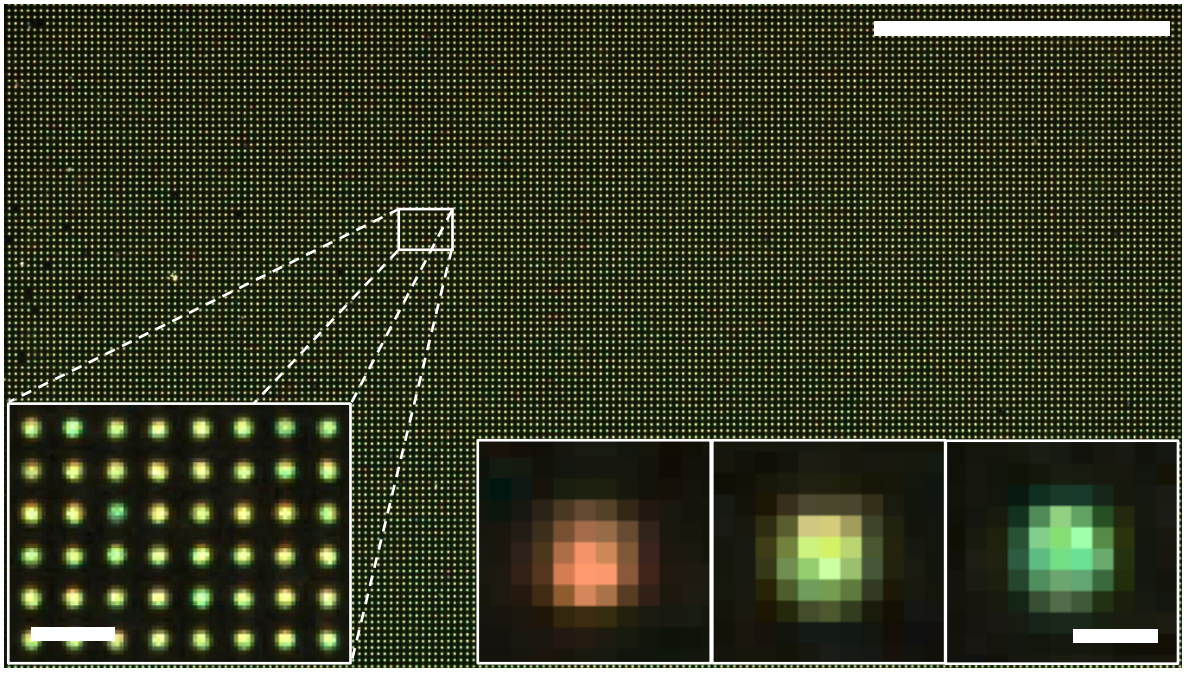

Fig. 4.2. One video frame of the DOTS platform. The field-of-view is 4.8mm by 2.7mm. (inset, bottom left) Zoomed in area of the DOTS device showing individual diffraction grating mirrors. (inset, bottom right) Different colors of the grating mirrors due to different tilting angles induced by the cells. Scale bars: (top left, 1.2 mm) (bottom right, 52 μm) (bottom right, 10 μm)

The zoomed in image show that the grating disks are distinctly separated from their neighbors with no overlap of light colors between disks. This ensures that there is negligible cross-talks between disks in the spatial domain.

4.2 Methods

4.2.1 Color to Tilt

In order to quantitatively extract out the color from the pixels of the camera, we need to assign a numerical index to the color, which is known as the hue. The hue, saturation, and value color space is widely used in the image editing industry. The hue can be calculated from the red, green and blue color space. Digital color cameras mainly work by having Bayer tile filters on the sensors of the camera. The most commonly used color filters correspond to the red, green, and blue primary colors respectively. Thus, each pixel can only detect one of the 3 primary colors.

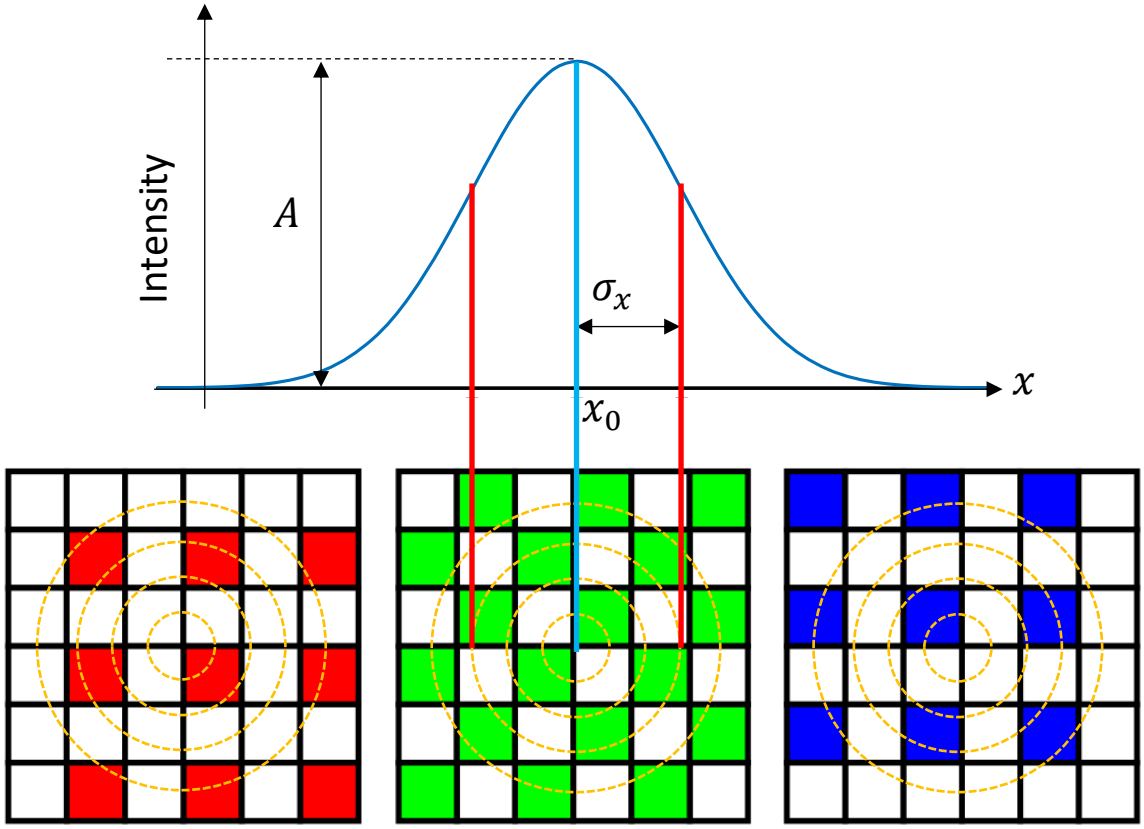

Fig. 4.3. Bayer tile pixels of the camera

Since the color sensors in most cameras are spatially offset from each other, the pixel intensity varies with the spatial location of the pixel (Fig. 4.3). This presents us with a dilemma:

Which pixel's intensity can we use to represent the true color intensity of the diffraction grating disk? In order to know the true color intensity of the center of each mirror disk, gaussian fitting was performed for each of the three-color tiles shown in Fig. 4.3. Gaussian fitting was used to determine the amplitude intensity of each of the red, green, and blue colors. Because the amplitude is not tied to any individual pixel, it is a good representation of the intensity of each of the RGB colors. Thus, three different amplitudes of the 2D gaussian were obtained, corresponding to each of the three primary colors. These three colored amplitudes were then converted to the hue, saturation and brightness color space using the standard MATLAB function.

To calibrate the relationship between the color and tilting angle of the device, we need a calibration tool to physically tilt a single diffraction grating disk in the center of the device. This is accomplished through the use of 2 tilting stages (goniometers), one in the x direction and one in the y direction. The device was placed into the sample holder and imaged through a camera lens.

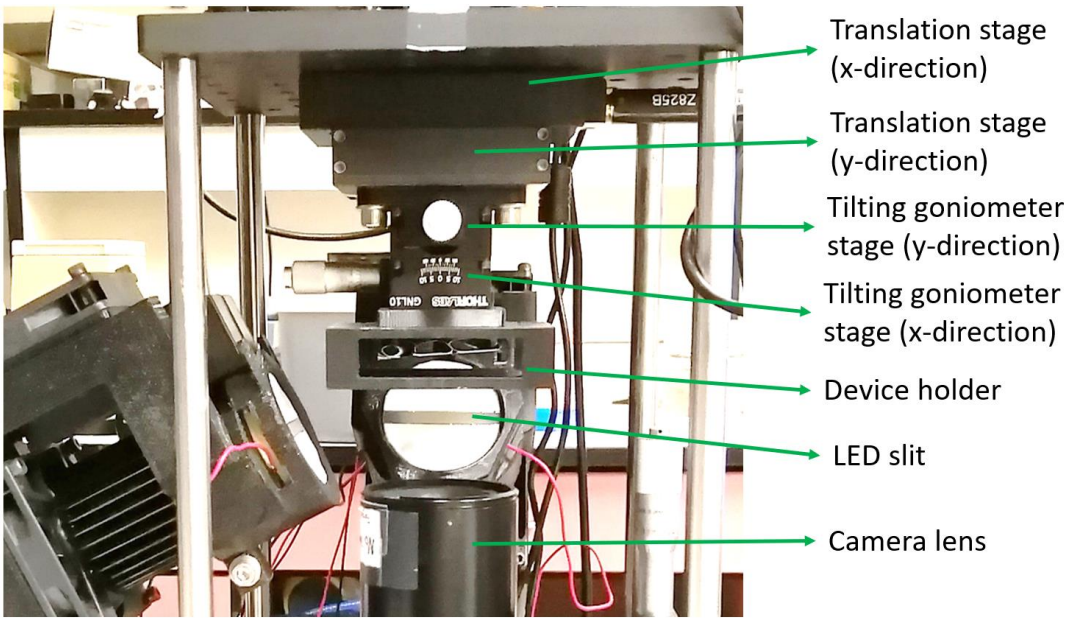

Fig. 4.4. Optics setup for imaging the DOTS device

The full optical setup for imaging the DOTS device comprises light emitting diodes (LEDs) (Citizen CLU550-3626C1), Canon MP-E 65mm f/2.8 1-5x Macro Photo lens set at 4x magnification, Chronos 2.1 HD high speed camera (Krontech), goniometers (GNL20, Thorlabs), and the integration of 3D printed plastic and metal parts as shown Fig. 4.4. The tilting goniometer stages were used for calibration of the color and tilt angles.

The goniometer was used to rotate the calibration DOTS device between angles of -4 to +4 degrees. To perform the calibration, the goniometer was tilted to a chosen angle. The light source illuminating in the y-direction was switched on while the light source in the x-direction was switched off. The camera & lens was then adjusted up and down to focus onto the geometrical center of the DOTS calibration device. The calibration image was then taken by the camera. A single grating disk in the center of the device was horizontally moved across the entire field of view, and imaged at different x & y spatial positions. Two micrometer translation stages (Fig. 4.4) were used to move the DOTS calibration device horizontally in the x and y directions while keeping its vertical position fixed at the focal plane. By moving the DOTS calibration horizontally, the calibration images were taken for different positions within the field-of-view of the camera. Nine different horizontal positions were imaged for each tilting angle, to form the dataset for calibration (Fig. 4.6(g)).

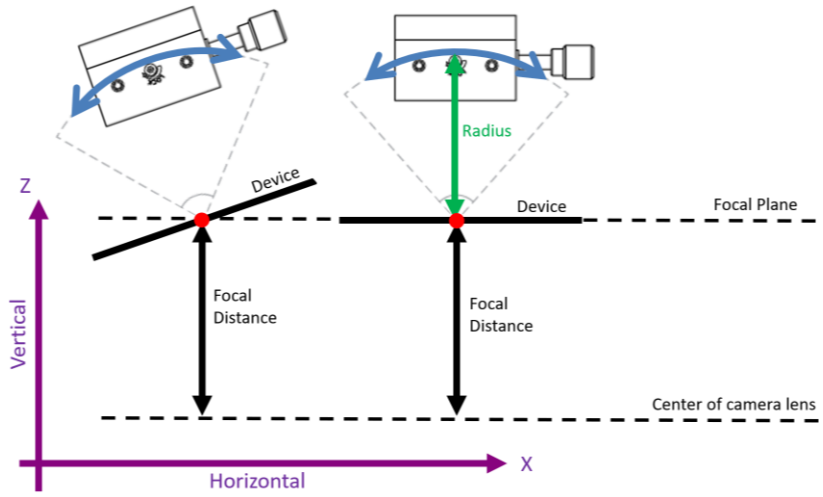

Fig. 4.5. Operation of tilting stage (goniometer)

Since the DOTS device is tilted due to the goniometer, only its geometrical center lies on the focal plane of the camera lens. Because the device was placed at a radial distance away from the tilting stage, when the stage is tilted, the center of the device denoted by the red circle in Fig. 4.5, remains at the same focal distance away from the camera lens. Even when the device is moved horizontally, the focal distance from the red circle Fig. 4.5 does not change. Therefore, by imaging only the same single grating disk in the center of the device denoted by the red circle Fig. 4.5, we were able to ensure that the focal plane does not change. Thus, this does not change any of the optics, except for the tilting angle of the disk which we are imaging.

The images from the calibration experiment were then computationally processed to extract the x & y coordinates and the hue value of the grating disks which were in focus at the focal plane. The equation of a hyper surface was fitted to the data points using the B-spline regression machine learning model (PyEarth). We consider the results of the calibration when the single disk is at the top left corner of the field of view, shown in Fig. 4.6(a)(b). The horizontal axis is the hue in the x-direction, while the vertical axis is the hue in the y direction. The color represents the tilting angle

of the disk. When the tilting angle in the x-direction changes from -3 degrees to +3 degrees, the hue changes from 0.2 to 0.4 as seen in Fig. 4.6(a). Similarly, when the tilting angle in the y-direction changes from -3 degrees to +4 degrees, the hue for the y-direction changes from 0.2 to 0.4 as seen in Fig. 4.6(b). The calibration relationship between the hue and tilting angles for positions at the center (Fig. 4.6(c)(d)) and at the bottom right (Fig. 4.6(e)(f)) of the field of view are also shown in Fig. 4.6(c)~(f). The gradient of the fitted background curve is different depending on which spatial position of the disk we are looking at. Since there are 6 variables here: the x & y spatial position, the 2-dimensional hue, and the 2-dimensional tilting angles, a machine learning approach was employed to fit these multi-dimensional background curves to the experimental data. The curving fitting error is plotted as a histogram in Fig. 4.6(h). The mean error is 0.22 degrees.

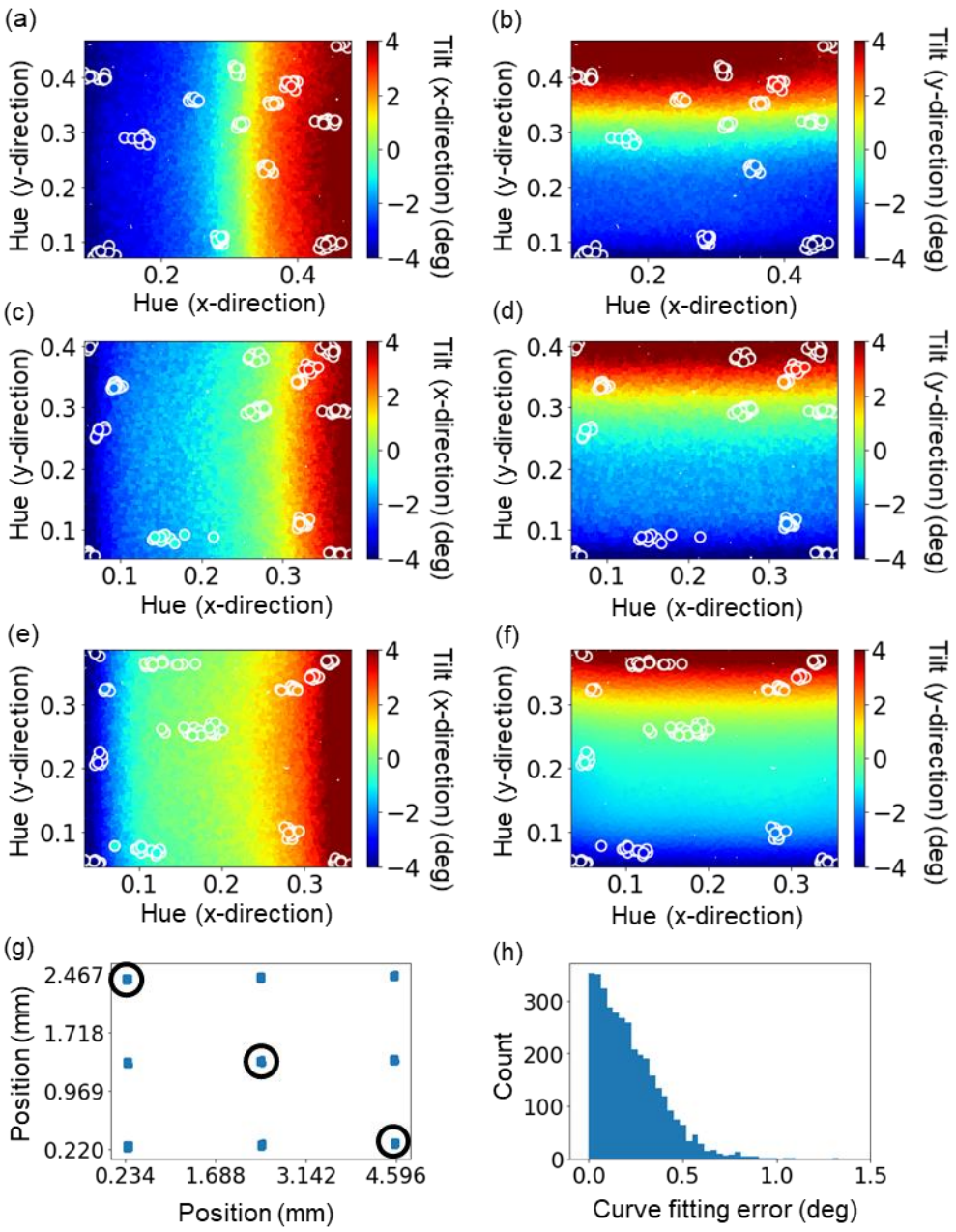

Fig. 4.6. Calibration of hue and tilt angle. (a)(b) Relationship between 2D hue and the tilting angles for the top left spatial position of the field-of-view. (c)(d) Relationship for the center spatial position of the field-of-view. (e)(f) Relationship for the bottom right spatial position. (g) Different spatial positions within the field-of-view for which data was taken. (h) Curve fitting error of the calibration data.

4.2.2 Fabrication

The DOTS devices were fabricated by starting with a silicon wafer with a 1.5 μm thermal dioxide layer. A 2D grating structure was then patterned onto the thermal dioxide layer using photolithography and dry etching (Fig. 4.7(a)). The thermal dioxide was then patterned and etched into isolated disks with a diameter of 10 μm (Fig. 4.7(b)). The photoresist used in the prior etching was kept as an etching mask for isotropic reactive ion etching of silicon (Fig. 4.7(c)). The photoresist was then removed using oxygen plasma. A composite metal layer consisting of 10nm Titanium, 100nm Aluminum, 10nm Titanium, and 100nm silicon dioxide was sequentially deposited on the oxide disks using electron beam evaporation (CHA Mark IV) (Fig. 4.7(d)). The rigid disks on silicon, and the PDMS substrate were exposed to oxygen plasma (500 mTorr, 75 Watts, 30 seconds, Technics RIE) before being mechanically bonded to each other (Fig. 4.7(e)). The bonded structure was placed into a beaker containing 55% acetone and 45% water. The beaker was then placed into an ultrasonic water bath to break the silicon neck at the interface between the oxide disks and silicon anchors (Fig. 4.7(e)), leaving the oxide grating disks (with metal) bonded on the PDMS substrate (Fig. 4.7(f)). The PDMS was then isotopically dry etched for 7mins (Oxford RIE), leaving a mushroom-like shape under the oxide grating disks (Fig. 4.7(g)). Fig. 4.8 shows the SEM image of the cross-section of a oxide disk on the DOTS platform.

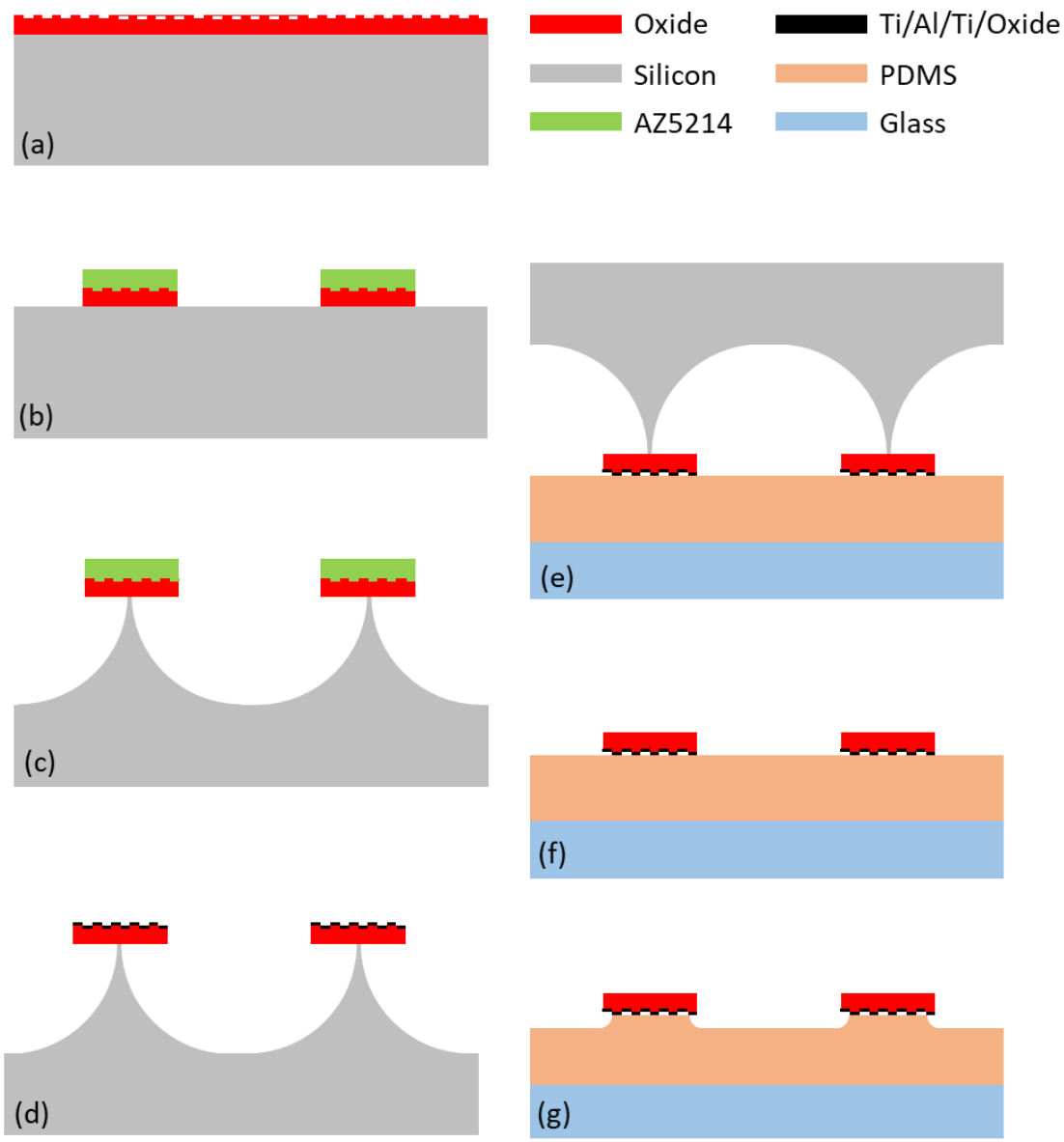

Fig. 4.7. Fabrication process flow of the DOTS device

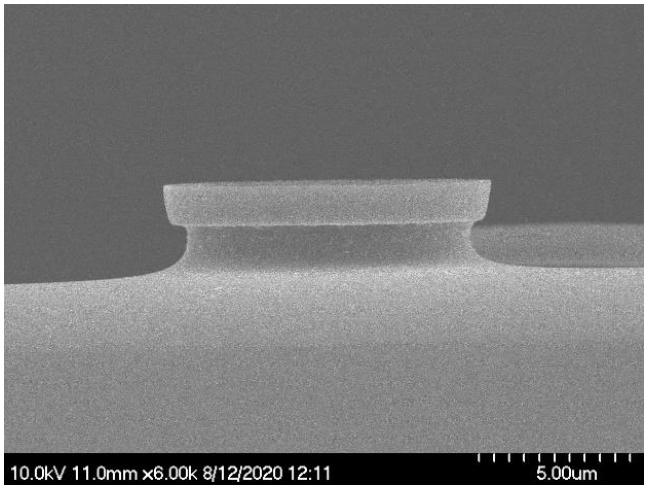

Fig. 4.8. Sidewall profile of a single DOTS micro-mirror after PDMS etching, taken by a scanning electron microscope.

4.2.3 PDMS Mechanical Properties Characterization

PDMS cylinders of diameter 25mm and height 17.74mm were made from mixing 6 parts of Sylgard 527 with 1 part of Sylgard 184 by mass. The PDMS liquid was poured into 3D printed plastic molds, and left to cure in the oven for 48 hours at 60 Celsius. The resulting PDMS cylinders were then subjected to uniaxial compression using the Instron 5960 machine (Fig. 4.9(a)). The stress-strain curves were then obtained from the Instron software which controlled the machine (Fig. 4.9(b)). We fitted a linear line to the region of the curve with strain less than 0.1 (Fig. 4.9(c)), in order to ensure that the young's modulus extracted from the gradient falls within the linear regime. The young's modulus measured was 197 kPa.

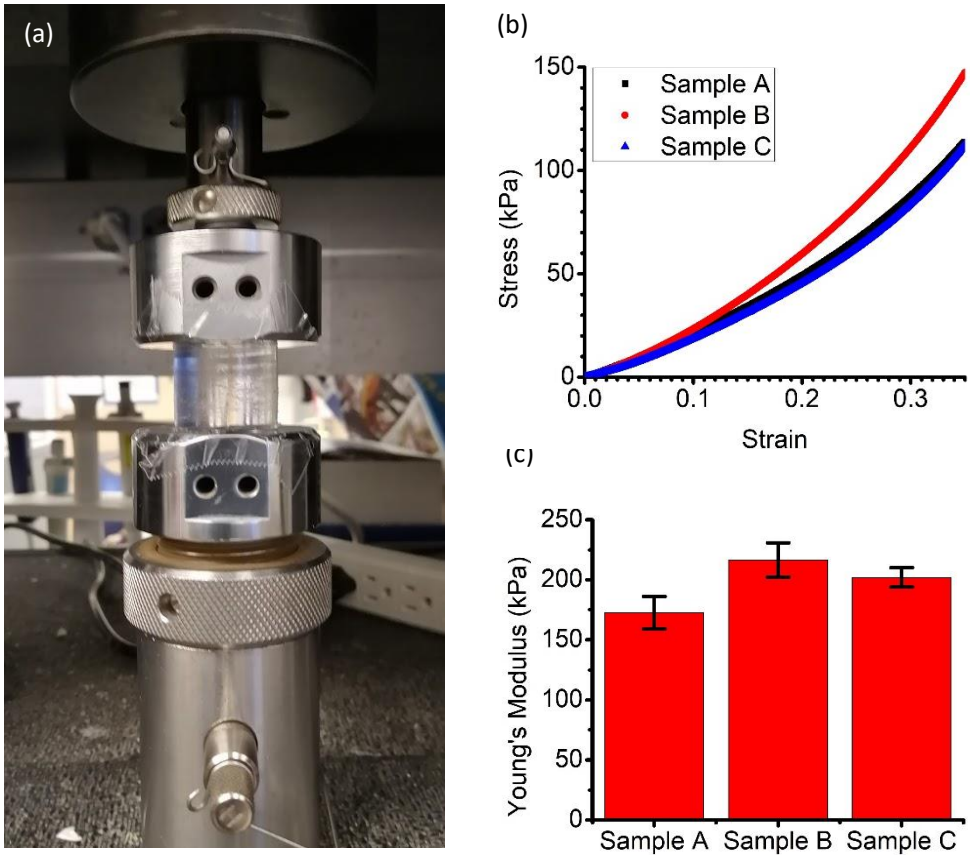

Fig. 4.9. Measurement of the Young's modulus of PDMS. (a) Uniaxial compression by Instron 5960 machine. (b) Stress strain curves of different PDMS samples. (c) Young's modulus of different PDMS samples.

4.2.4 Extraction of Traction Stress Distribution

In order to extract the traction stresses from the measured tilting angle information on DOTS, we apply a machine learning model to predict the traction stress distribution from the tilting angles of the disk array as illustrated in Fig. 4.10. This machine learning model requires training data in the form of random traction stresses generated by a Fourier series, and tilting angles calculated by the COMSOL mechanics simulation. The COMSOL mechanics simulation requires

the information of the device geometry (see Chapter 4.2.3 above), as well as the Young's modulus of the materials including PDMS.

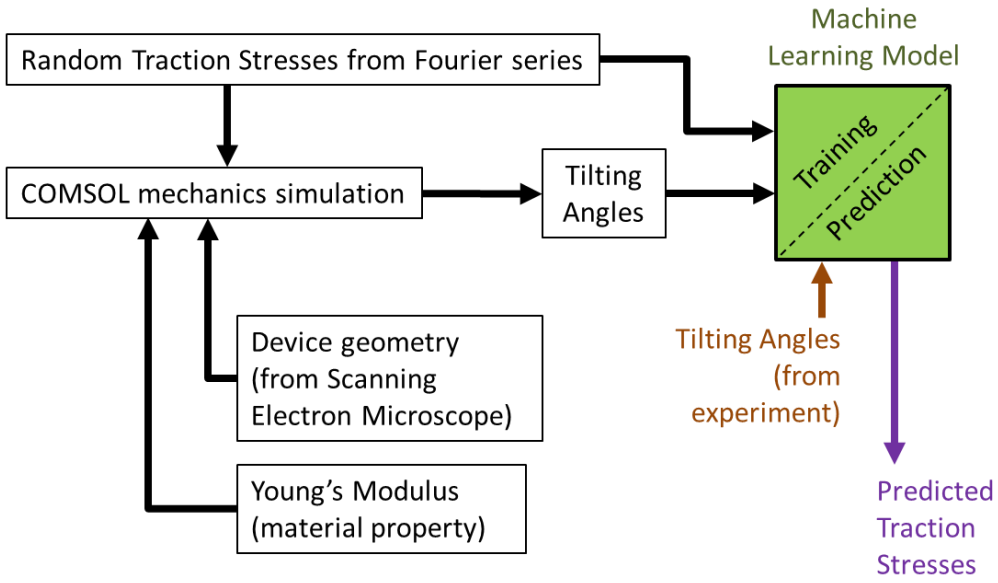

Fig. 4.10. Data process flow of training and prediction using machine learning.

Since the grating disks are mounted on a continuous PDMS film, there exists mechanical coupling between neighboring disks when traction forces are applied. To extract the traction force distribution information from the measured tilting angles of disks on DOTS, we used COMSOL to generate training data to train a linear regression machine learning model (scikit-learn). Random stress distributions were generated from a 2-dimensional Fourier series, using random numbers for the amplitude and phase terms, according to equation 2.

$$Stress(x,y) = \sum_{-n}^{n}\sum_{-m}^{m} A_{m,n}\cos[w(mx+ny)+\phi] \qquad (eqn\ 2)$$

$$\text{where} \quad w = \frac{2\pi}{\lambda} = 2\pi f$$

$$\lambda = 1.8 \text{ mm}$$

$$A_{m,n}\ and\ \phi \text{ are random numbers}$$

A total of 2000 different random stress distributions were imported into the COMSOL mechanics simulation to calculate the corresponding tilting angles of a 5 x 5 array of disks in the DOTS platform. One example random stress distribution is shown in Fig. 4.11(a). This stress distribution causes vertical displacement of the 5 x 5 disk array shown in Fig. 4.11(b). The tilting angles were calculated from the vertical displacements using simple trigonometry. A total of 2000 pairs of random stress distributions and tilting angle arrays were generated from COMSOL, and were used to train the linear regression machine learning model (sci-kit learn).

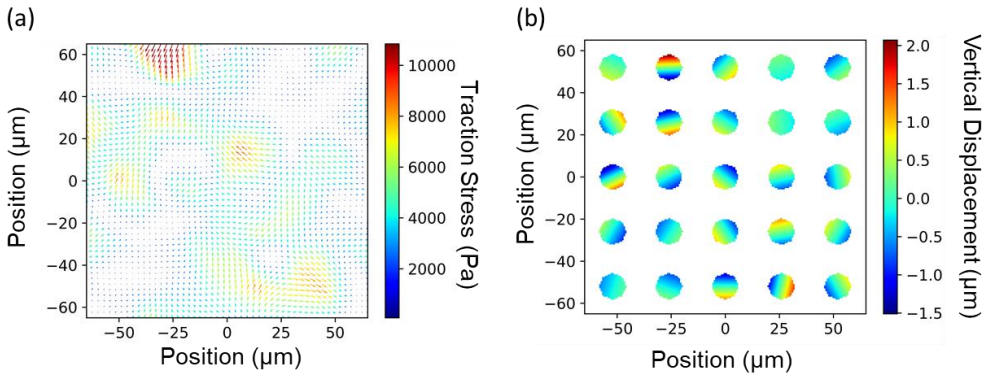

Fig. 4.11. Training data for machine learning. (a) One example of random stress distribution. (b) Corresponding vertical displacements of the disks array solved by COMSOL.

As the machine learning package could only take in data in the format of rows and columns, there was a need to transform the 2D spatially varying stress and tilting angle distributions into the format of columns. If we look at a small area in the spatially varying traction stress plot, the small area can be divided into a grid, with many grid points, as shown in Fig. 4.12.

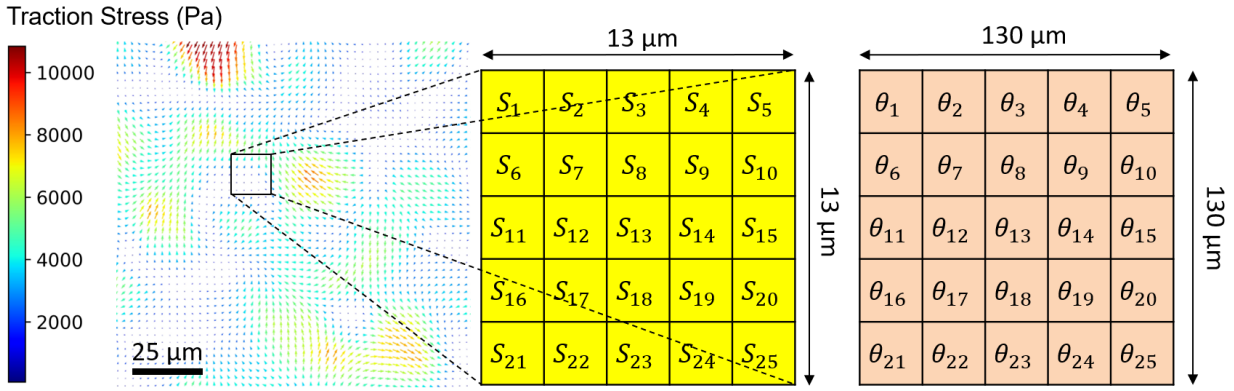

Fig. 4.12. Division of spatial areas into grid points

Every point in the grid can be mapped to 2 columns in the data table, with the 1st column representing the x component of the stress (S_{x1}), the 2nd column representing the y component of the stress (S_{y1}) as shown in Fig. 4.13. Therefore, every grid point is being mapped to 2 columns in the data table. The same mapping from grid points to columns was done for the spatially varying tilting angles.

Instances (scenarios)	Traction Stress (kPa)						Tilt Angles (deg)					
n	S_{x1}	S_{y1}	S_{x2}	S_{y2}	$S_{x...}$	$S_{y...}$	θ_{x1}	θ_{y1}	θ_{x2}	θ_{y2}	$\theta_{x...}$	$\theta_{y...}$
1												
2												
...												
2000												

Fig. 4.13. Data table for import into machine learning model

The 2000 rows in the data table correspond to the 2000 different scenarios of random stresses and tilting angles used to train the machine learning model. The trained machine learning model can be used to predict stress distribution from tilting angles obtained from experiments. ,

The field of view of the DOTS platform spans over 13 mm^2. However, the COMSOL mechanics simulation used to generate the training data only spanned an area 130 x 130 μm^2. Therefore, we have to use a stepping method to step an area of 5 x 5 disks over the entire field of view.

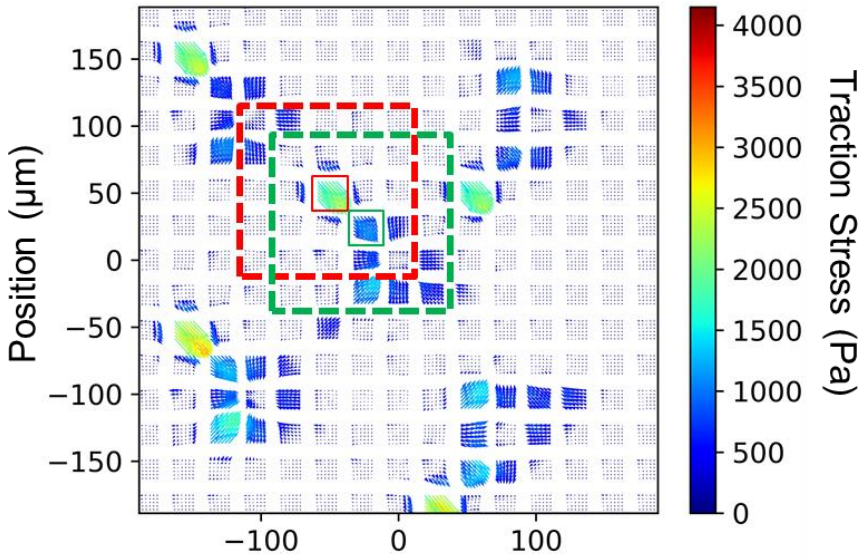

Fig. 4.14. Splitting of a large area from the field-of-view into smaller areas each spanning 130μm by 130μm.

We used 25 tilting disks bounded by the red dotted box in Fig. 4.14 to predict the traction stress in the center area bounded by the small red box. By moving the red dotted box to the position of the green dotted box, another 25 disks are used to predict the traction stress in the center area bounded by the small green box. Therefore, by stepping the dotted boxes over the entire field of

view, the full traction stress distribution over the entire simulated area spanning 494μm by 494μm is reconstructed. The traction force distribution missing between boxes are filled by interpolation.

4.2.5 Validation of the machine learning approach with known stress distribution

In order to know if this machine learning model can predict accurate traction stress distribution, we test the model with a known experimental stress distribution adapted from the prior work published by Zeinab et al [143]. The known stress distribution were imported into the COMSOL mechanics simulation to solve for the simulated tilting angles as illustrated in Fig. 4.15. The tilting angles are then fed into the machine learning model to predict the traction stresses. If the machine learning model is reliable, the predicted stress distribution is expected to match the known experimental stress distribution.

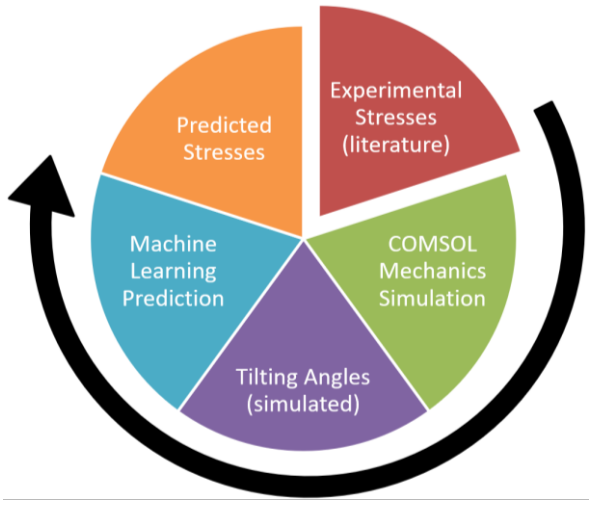

Fig. 4.15. Data process flow for validating the machine learning model with a known stress distribution

The known experimental stresses adapted from Zeinab et al [143] are shown in Fig. 4.16(a). The traction stresses predicted by the machine learning model is shown in Fig. 4.16(b).

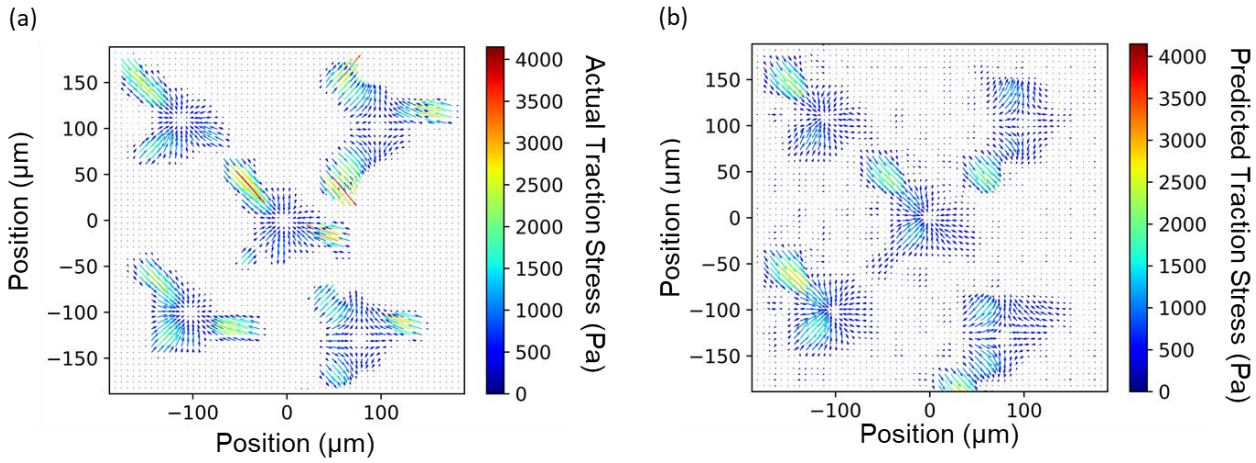

Fig. 4.16. Traction stresses used to validate the machine learning model. (a) True known experimental stresses adapted from Zeinab et al [143]. (b) Stresses predicted by the machine learning model.

It is observed that the sub-cellular resolution of the traction stresses (Fig. 4.16(b)) is preserved in the predicted stresses, while some regions inside the cells are not perfectly replicated. In fact, the predicted stresses show some smoothing of the stress features. This can be explained by the fact that a limited number of Fourier terms were used in the simulated data (Fig. 4.11) used for training the machine learning model. Therefore, some high spatial frequency terms were lost in the predicted stresses. Statistical errors were calculated by taking the difference in the vector components of the known (Fig. 4.16(a)) and predicted stresses (Fig. 4.16(b)), and plotted as a histogram in Fig. 4.17. The mean error is 538 Pa while the median error is 400 Pa. The median error expressed as a percentage of the maximum traction stress is 9.8%.

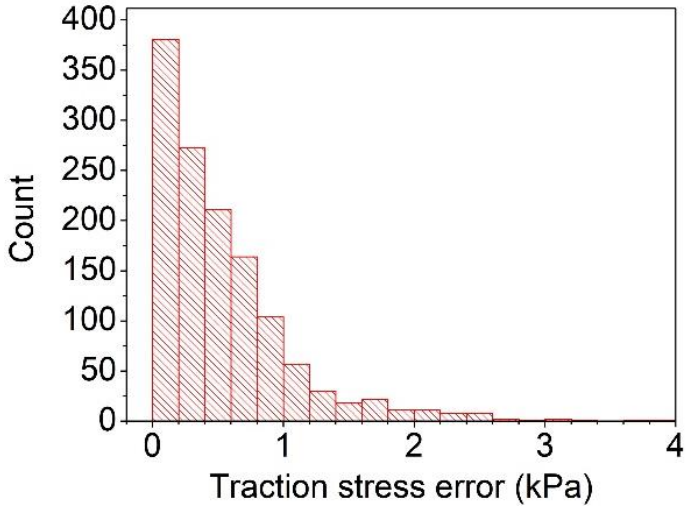

Fig. 4.17. Errors calculated by taking the vector differences between the known and predicted stresses.

4.3 Results & Discussion

4.3.1 Traction stress

To visualize the peak traction stresses of a continuous sheet of rat cardiomyocytes, four video frames were chosen. Two of the chosen video frames, which we call the background frames, corresponded to the x and y tilting angles of the point in time when the cardiomyocytes were not beating. The other two video frames, which we call the beating frames, correspond to the x and y tilting angles of the point in the time when the cardiomyocytes were at the peak of the cardiac beat. The background video frames were subtracted from the beating video frames to obtain the instantaneous dynamic traction stresses of the cardiac beat. For efficiency in computational processing, the entire field-of-view of 13mm² was split into many small areas, each spanning 130µm x 130µm. The 2-dimensional tilting angles extracted from experiment were then fed into the machine learning model, which then predicted the corresponding peak traction stress distribution over the entire field-of-view shown in Fig. 4.18.

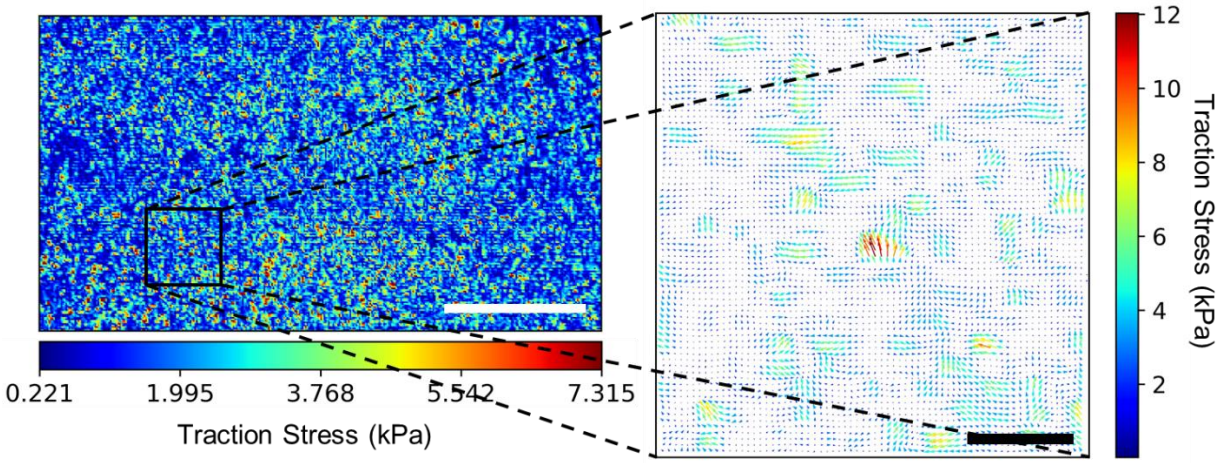

Fig. 4.18. Traction Stresses predicted by machine learning model. (a) Entire field-of-view spanning 4.8mm x 2.7mm. Scale bar: 1.2 mm. (b) Traction stresses of zoomed in area. Scale bar: 125 µm.

The stresses in this small box on the left of Fig. 4.18 are zoomed in and plotted on the right figure. As the cells are tightly packed in a continuous tissue sheet, the individual cells cannot be distinguished from each other in this traction stress plot.

In order to know whether these predicted traction stresses are accurate, we import the predicted stresses back into the COMSOL mechanics simulation, to solve for the validated tilting angles (Fig. 4.19). If the predicted stresses are correct, the validated tilting angles should match the experimental tilting angles.

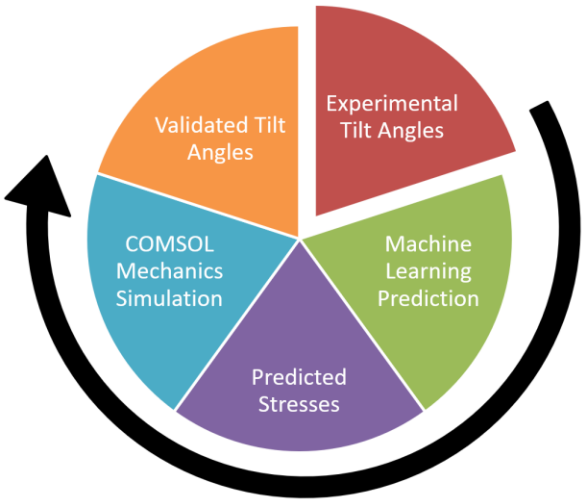

Fig. 4.19. Data process flow for validation of machine learning model from known tilting angles

In order to quantify the errors of the prediction, the predicted stresses in Fig. 4.18 were split into many small regions each spanning 130μm x 130μm, corresponding to an area of 5 x 5 array of disks. A random sample of the multitude of small regions were imported into COMSOL, and the corresponding tilting angles of the grating disks were then solved. The corresponding validated tilting angles from the COMSOL mechanics simulation are shown in Fig. 4.20(b). The validated tilt angles Fig. 4.20(b) were then compared to the actual tilt angles obtained from

experiment (Fig. 4.20(a)). The two plots match well, proving that the machine learning model is reliable.

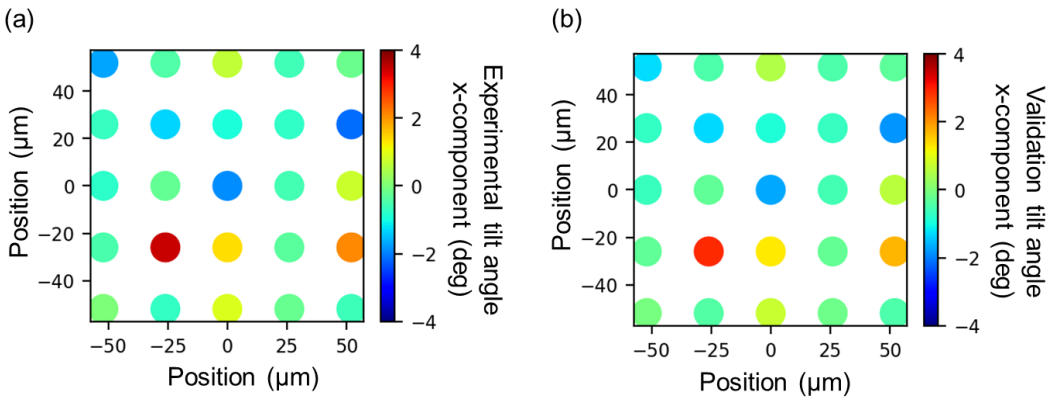

Fig. 4.20. Tilting angles of a chosen 5x5 array of micro-mirror disks. (a) Tilting angles from experiment. (b) Validated tilting angles from COMSOL simulation of predicted stresses.

Since the tilting angles from an array of 5 x 5 disks were used to predict the traction stress in the small dotted red box in the center (as previously explained in Fig. 4.14), we calculate the error of the tilting angle by considering only the difference between the tilting angles of the center disks in these two plots. Many such small areas over the entire field of view were randomly sampled to calculate the error plotted as a histogram in Fig. 4.21. The median error obtained is 0.29 degrees, which when expressed as a percentage of the maximum tilting angle, gives us a median percentage error of 7.25 %.

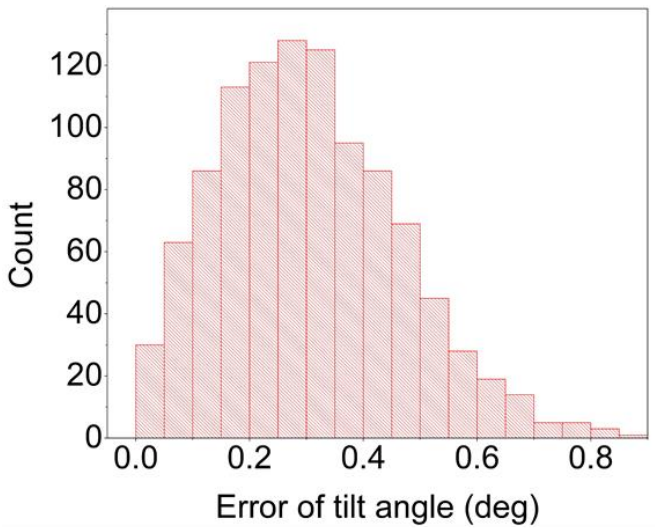

Fig. 4.21. Statistical distribution of the error of a random sample of disks

4.3.2 Mechanical wave propagation measured on DOTS

The tilting angles from the non-beating background video frame were subtracted from the other video frames, to obtain the change in tilting angles due to the cardiac beat of cardiomyocytes. The dynamic tilting angles were then interpolated over the entire field-of-view as shown in Fig. 4.22.

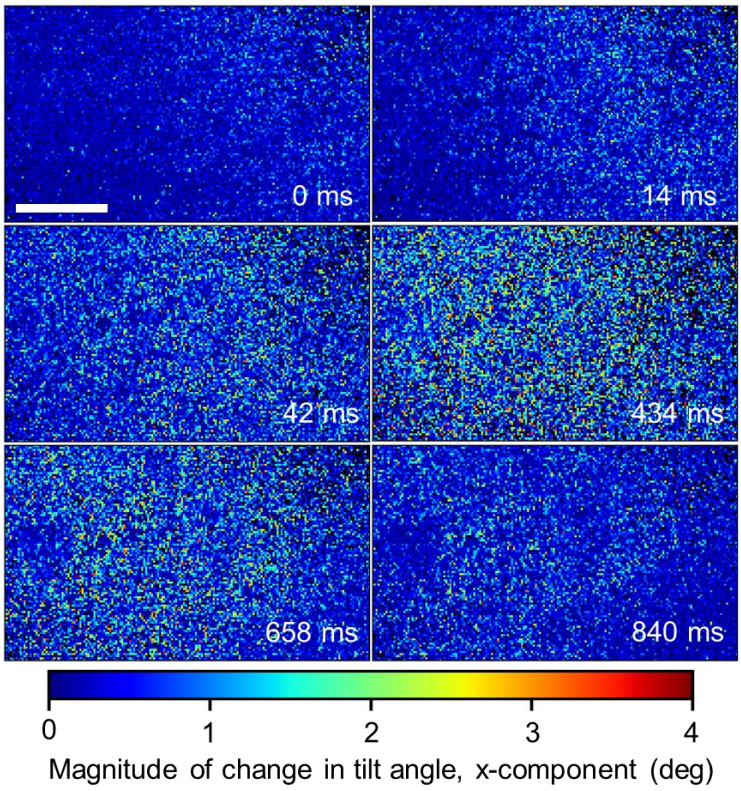

Fig. 4.22. Propagation of cardiac beat across the entire field-of-view. Scale bar: 1.2mm.

Selected video frames capturing the propagation of a single cardiac beat are shown in Fig. 4.22. This plot shows the magnitude change in the tilting angle at different snapshots in time. The frame rate of the video was 71 frames per second. As time progresses, the cardiac beat propagates from the right to the left of the field of view. At 434ms, the entire field of view is activated with the maximum change in tilting angle. The cardiac beat incompletely subsides at 840ms.

The concept of the activation time must first be considered, before the results of the mechanical wave can be explored. We assume that the entire area in Fig. 4.23(a) is filled up with cardiomyocyte tissue. Within a single cardiac beat, the mechanical wave propagates from the top right corner to the bottom left corner of the entire tissue area in Fig. 4.23(a). When the traction stress over time is plotted for different spatial locations of the area, namely the location at A, B and C in Fig. 4.23(a), the traction stress is observed to increase to the peak of the beat (Fig. 4.23(b)), before decreasing when the cardiac beat is past.

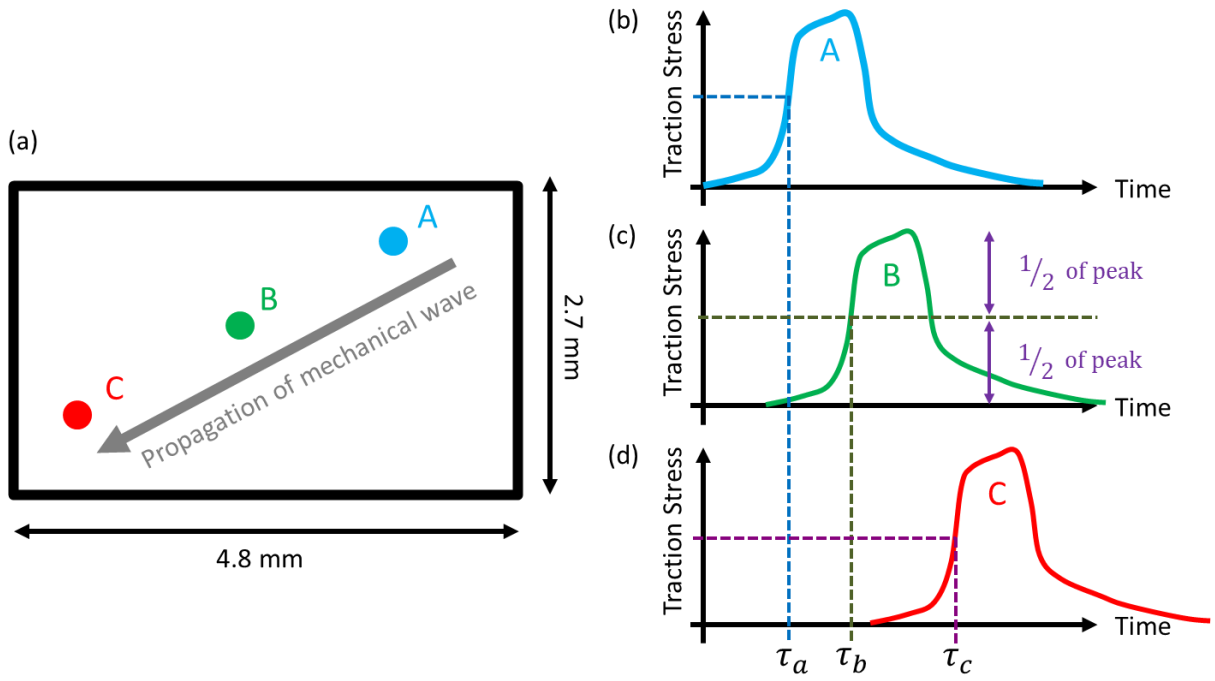

Fig. 4.23. Concept of activation time

The activation time which represents the exact time of the cardiac beat at each spatial location, is defined as timing of the maximal time derivative of the signal [144] [145] [146]. This is the same as the time at which the gradient of the curve is the steepest, denoted by the colored dotted lines in Fig. 4.23(b)(c)(d). This also corresponds to the mid-point of the peak traction stress as labelled in Fig. 4.23(c). We can see that the activation times τ_A , τ_B , τ_C are different, depending

on which spatial location of the tissue area we are looking at. The activation time tells us the exact time at which the mechanical wave passes through each spatial location.

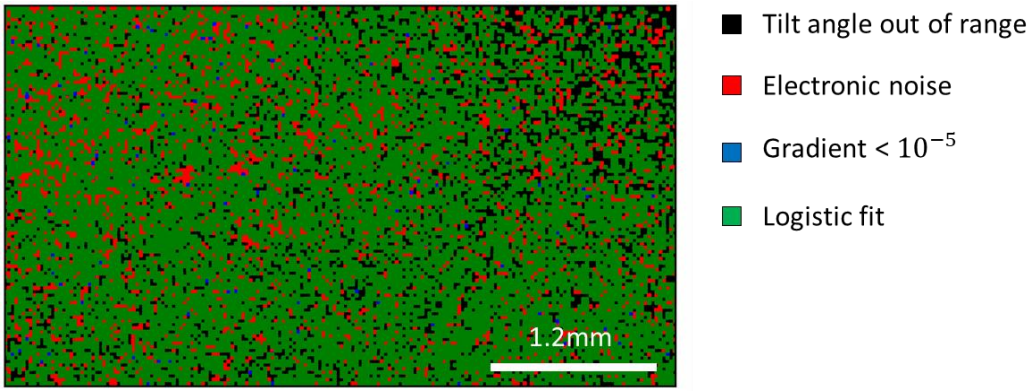

Fig. 4.24. Categories of the time dependent traction stress profile.

In order to extract the activation time from the experimental data, the traction stress of every micro disk in the field of view was plotted against time. The time dependent profile of three representative disks is plotted in Fig. 4.25. For the majority of the disks denoted by the color green plotted in this field-of-view (Fig. 4.24), their time dependent traction stress profile fits very well to the logistic function. This allows us to extract the activation time from the mid-point of the maximum change in traction stress as exemplified in Fig. 4.25(c). A sharp gradient exists at the center of the plot from which the activation time can be extracted from the vertical mid-point (see green dotted lines) of the logistic curve. The activation time is at about 300ms in Fig. 4.25(c). For a small number of disks denoted by the color blue in the field-of-view (Fig. 4.24), the traction stress changes very slowly over time as exemplified in Fig. 4.25(b). The dimensionless gradient ($< 10^{-5}$) of the logistic function fitted over the data is extremely small. Thus, the gradient of the plot is too gentle for us to extract any meaningful activation time from the data. Some of the disks which are plotted in red in the field-of-view (Fig. 4.24), do not have any noticeable change in the

traction stress over time. The data from such disks is dominated by electronic noise as shown in Fig. 4.25(a). Therefore, they do not fit the logistic function, and no activation time can be extracted from these areas shown in red. The remaining areas shown in black (Fig. 4.24) correspond to disks which have tilting angles beyond ±4 degrees, which is outside of the calibration range. No data can be extracted from them.

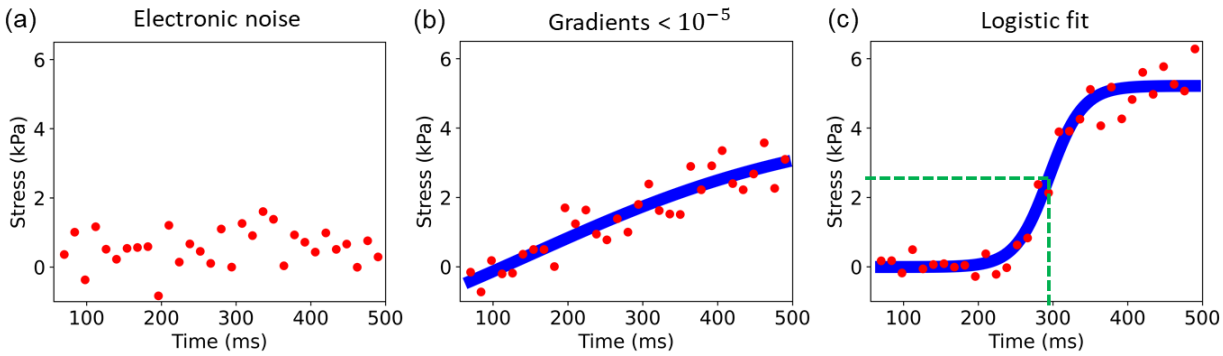

Fig. 4.25. Propagation of cardiac beat across the entire field-of-view. Scale bar: 1.2mm.

The activation times for the disks which do fit the logistic function are plotted as colors over the entire field of view for both the control experiment shown in Fig. 4.26(a) and also for the experiment with the drug phenylephrine in Fig. 4.26(b). Areas plotted in white represent disks from which no activation time can be extracted (as previously explained in Fig. 4.25), as well as the disks outside the calibration range. For the experiment where the drug phenylephrine was added, the video was taken 40mins after adding the drug. Phenylephrine is known to cause adrenergic activation of cardiomyocytes [147], which in turn causes hypertrophy [148] [149]. We can see the addition of the drug severely disrupts the mechanical wave, because vastly varying activation times represented by the red and blue colors are interspersed over the entire area in Fig. 4.26(b). Consequently, there is no clear direction of the propagation of the mechanical wave. It is

unknown why phenylephrine-induced adrenergic activation disrupts the mechanical wave, and this remains to be discovered by biologists in the future. The range of activation times was calculated by taking the difference between the maximum and minimum activation times in the color bars of Fig. 4.26(a)(b). It represents the total time taken for the entire field-of-view to activate fully mechanically. The range of activation times in Fig. 4.26(b) for the drug experiment is 303ms, which is a much wider range than in Fig. 4.26(a) for the control experiment of 94ms. This shows that the drug phenylephrine is causing the neonatal rat ventricular myocyte (NRVM) tissue to take a longer time to fully activate. The drug also destroys the ability of the cells to beat in a coherent way.

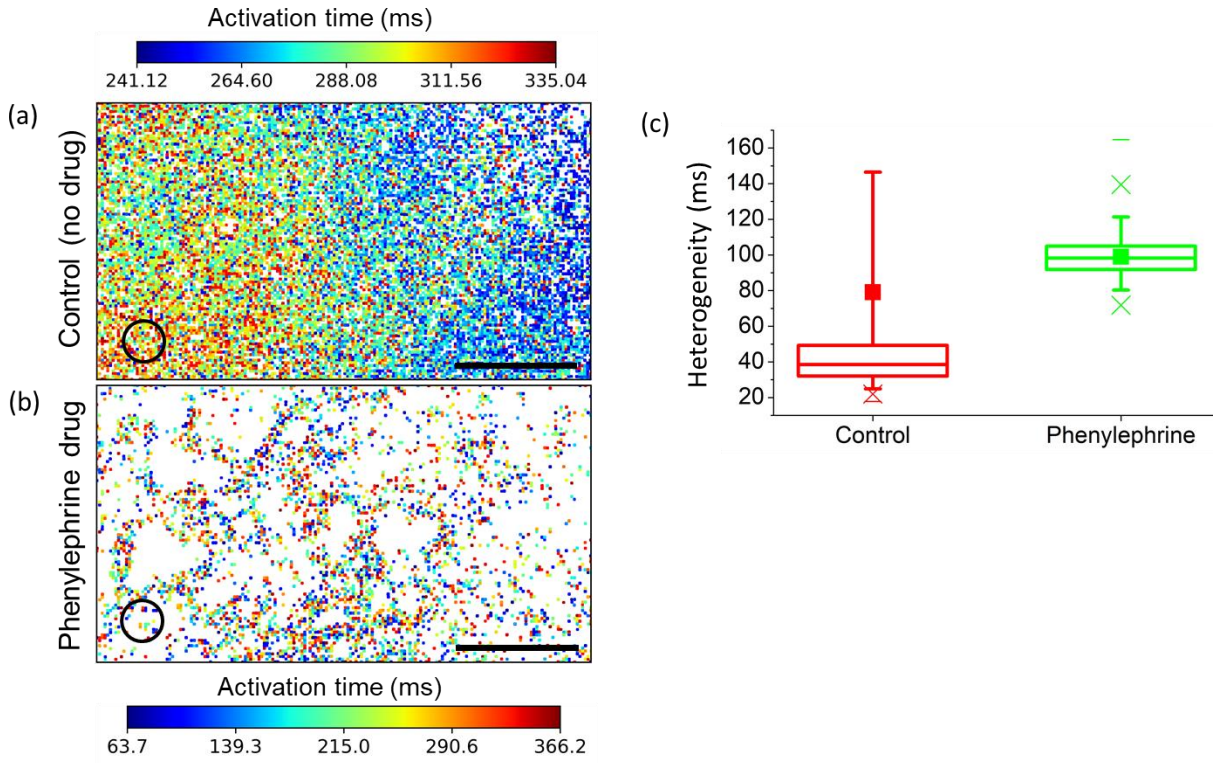

Fig. 4.26. Activation time of neonatal rat ventricular myocytes (NRVM). (a) Activation time plot from control experiment with no drug. (b) Activation time plot 40mins from adding the drug

phenylephrine. (c) Comparison of the heterogeneity of the activation time, which is the standard deviation of the activation time within an area of radius 200 microns. Scale bars: 1.2 mm.

The activation times in Fig. 4.26(a) for the control experiment with no drug generally show earlier activation times on the right and later activation times on the left of the entire field-of-view. This reveals that the mechanical wave of the cardiac beat is generally propagating from the upper right to the bottom left. Even for the control experiment, the activation times within a small area of radius 200 microns is heterogenous. The interspersing of red and blue colors can be seen even within small local regions from the control experiment (Fig. 4.26(a)). In order to quantify the spatially heterogeneous phenomenon of the activation time, we define heterogeneity as the standard deviation of the activation time within a spatial radius of 200 microns. The heterogeneity has the same units as the activation time. The heterogeneity was calculated for disks with logistic fit over the entire field-of-view and plotted in Fig. 4.26(c). The heterogeneity is a measure of the failure of neighboring cells to be coherently activated. Therefore, it can be used to quantify how likely the cells and tissue are prone to causing arrythmia. As seen in the statistical box plot in Fig. 4.26(c), the introduction of the drug phenylephrine greatly increases the heterogeneity, thus severely increasing the risk of arrythmia in the tissue.

Chapter 5 Conclusion

Several technologies for achieving large field-of-view measurements of cell traction stresses have been discussed. The gold disk mounted micro-pillars and gold nanoparticles in flat PDMS platforms are able to achieve fields-of-view up to 894μm × 670μm under 10x magnification, whilst preserving sub-cellular resolution.

The Diffractive Optical Tracers (DOTS) platform extends the field-of-view to 4.8mm by 2.7mm under 4x magnification, and also preserved sub-cellular resolution using diffractive micro-mirrors with a pitch of 26 μm. Additionally, the DOTS platform is able to achieve concurrent videography up to a frame rate of 71 frames per second per direction for detecting mechanical waves of cardiac beat. The DOTS platform is bio-compatible, as proven by the maintenance of primary mammalian neonatal rat ventricular myocytes as a connected tissue sheet on the platform.

To further improve on the performance of the DOTS platform, the pitch between the diffraction grating disks can be further reduced below 26 μm, to improve upon the sub-cellular resolution which we have already achieved. A high-speed camera with more pixels in the imaging sensor can be used. To reduce electronic noise and increase the frame rate in our measurements, larger heat sinks and fans can also be used to cool down the LEDs, so that the LEDs can be operated at higher currents to produce higher luminance.

For future work, magnetic materials can be added to the devices of all the above-mentioned platforms. For example, a rod of magnetic particles has already been embedded along the length of the PDMS micro-pillars by Sniadecki *et al* [150]. By integrating the magnetic function into the gold disk mounted micro-pillars, a variety of functions such as cell stimulation and cell stiffness measurement can be expanded to large field-of-view.

Another way to measure the cell stiffness is to embed magnetic particles onto or into a continuous PDMS substrate, analogous of the embedding of gold nanoparticles into continuous PDMS demonstrated in chapter 3. Tseng *et al* [151] demonstrated a platform integrating magnetic nanoparticles into a continuous polymer film for stimulating cells. However, the function of extracting the cell stiffness was neither claimed nor achieved. This is due to the mechanical complexity of the problem which requires the use of reverse finite element methods using machine learning. However, with our recent advances in computational methods, we believe the back-calculation of the cell stiffness is now possible.

By using soft magnetic particles with zero remanence as similarly demonstrated by Optical Magnetic Twisting Cytometry (OMTC) [76], the frequency-dependent cell stiffness parameters can be extracted to precisely distinguish between various cell types [152]. The idea of introducing magnetic materials into DOTS was explored by Chiou *et al* [153]. This will expand the applications of the DOTS platform to include both sub-cellular stiffness measurements and cell stimulation, whilst maintaining our existing advantages of large field-of-view and high frame rate.

References

[1] E. Moeendarbary and A. R. Harris, "Cell mechanics: principles, practices, and prospects," *Wiley Interdisciplinary Reviews: Systems Biology and Medicine,* vol. 6, p. 371–388, 7 2014.

[2] J. Chen, J. Irianto, S. Inamdar, P. Pravincumar, D. A. Lee, D. L. Bader and M. M. Knight, "Cell Mechanics, Structure, and Function Are Regulated by the Stiffness of the Three-Dimensional Microenvironment," *Biophysical Journal,* vol. 103, pp. 1188-1197, 2012.

[3] D. A. Lee, M. M. Knight, J. J. Campbell and D. L. Bader, "Stem cell mechanobiology," *Journal of Cellular Biochemistry,* vol. 112, pp. 1-9, 2011.

[4] D. E. Ingber, L. Dike, L. Hansen, S. Karp, H. Liley, A. Maniotis, H. McNamee, D. Mooney, G. Plopper, J. Sims and N. Wang, "Cellular Tensegrity: Exploring How Mechanical Changes in the Cytoskeleton Regulate Cell Growth, Migration, and Tissue Pattern during Morphogenesis," in *Mechanical Engineering of the Cytoskeleton in Developmental Biology*, vol. 150, R. Gordon, Ed., Academic Press, 1994, pp. 173-224.

[5] F. Lautenschläger, S. Paschke, S. Schinkinger, A. Bruel, M. Beil and J. Guck, "The regulatory role of cell mechanics for migration of differentiating myeloid cells," *Proc Natl Acad Sci USA,* p. pnas.0811261106, 8 2009.

[6] C. M. Nelson, R. P. Jean, J. L. Tan, W. F. Liu, N. J. Sniadecki, A. A. Spector and C. S. Chen, "Emergent patterns of growth controlled by multicellular form and mechanics," *Proc Natl Acad Sci U S A,* vol. 102, p. 11594, 8 2005.

[7] S.-Y. Tee, A. R. Bausch and P. A. Janmey, "The mechanical cell," *Current Biology,* vol. 19, pp. R745-R748, 2009.

[8] C. M. Kraning-Rush, J. P. Califano and C. A. Reinhart-King, "Cellular Traction Stresses Increase with Increasing Metastatic Potential," *PLOS ONE,* vol. 7, pp. 1-10, 2 2012.

[9] Y.-T. Yeh, R. Serrano, J. François, J.-J. Chiu, Y.-S. J. Li, J. C. del Álamo, S. Chien and J. C. Lasheras, "Three-dimensional forces exerted by leukocytes and vascular endothelial cells dynamically facilitate diapedesis," *Proceedings of the National Academy of Sciences,* vol. 115, p. 133–138, 2018.

[10] B. Vianay, F. Senger, S. Alamos, M. Anjur-Dietrich, E. Bearce, B. Cheeseman, L. Lee and M. Théry, "Variation in traction forces during cell cycle progression," *Biology of the Cell,* vol. 110, pp. 91-96, 2018.

[11] D. Ingber, "Mechanobiology and diseases of mechanotransduction," *Annals of Medicine,* vol. 35, pp. 564-577, 2003.

[12] D. A. Affonce and K. R. Lutchen, "New perspectives on the mechanical basis for airway hyperreactivity and airway hypersensitivity in asthma," *Journal of Applied Physiology,* vol. 101, pp. 1710-1719, 2006.

[13] J. Klein-Nulend, R. G. Bacabac, J. P. Veldhuijzen and J. J. W. A. V. Loon, "Microgravity and bone cell mechanosensitivity," *Advances in Space Research,* vol. 32, pp. 1551-1559, 2003.

[14] M. A. Vollrath, K. Y. Kwan and D. P. Corey, "The Micromachinery of Mechanotransduction in Hair Cells," *Annual Review of Neuroscience,* vol. 30, pp. 339-365, 2007.

[15] M. A. GIMBRONE JR., J. N. TOPPER, T. O. B. I. NAGEL, K. R. ANDERSON and G. U. I. L. L. E. R. M. O. GARCIA-CARDEÑA, "Endothelial Dysfunction, Hemodynamic Forces, and Atherogenesisa," *Annals of the New York Academy of Sciences,* vol. 902, pp. 230-240, 2000.

[16] M. J. Paszek, N. Zahir, K. R. Johnson, J. N. Lakins, G. I. Rozenberg, A. Gefen, C. A. Reinhart-King, S. S. Margulies, M. Dembo, D. Boettiger, D. A. Hammer and V. M. Weaver, "Tensional homeostasis and the malignant phenotype," *Cancer Cell,* vol. 8, pp. 241-254, 2005.

[17] S. Judex, T. S. Gross, R. C. Bray and R. F. Zernicke, "Adaptation of bone to physiological stimuli," *Journal of Biomechanics,* vol. 30, pp. 421-429, 1997.

[18] J. C. H. Tan, F. B. Kalapesi and M. T. Coroneo, "Mechanosensitivity and the eye: cells coping with the pressure," *British Journal of Ophthalmology,* vol. 90, p. 383–388, 2006.

[19] A. Heydemann and E. M. McNally, "Consequences of Disrupting the Dystrophin-Sarcoglycan Complex in Cardiac and Skeletal Myopathy," *Trends in Cardiovascular Medicine,* vol. 17, pp. 55-59, 2007.

[20] T. P. Stossel, "On the crawling of animal cells," *Science,* vol. 260, p. 1086–1094, 1993.

[21] D. E. Ingber, D. Prusty, Z. Sun, H. Betensky and N. Wang, "Cell shape, cytoskeletal mechanics, and cell cycle control in angiogenesis," *Journal of Biomechanics,* vol. 28, pp. 1471-1484, 1995.

[22] S. R. Heidemann and R. E. Buxbaum, "Mechanical tension as a regulator of axonal development," *Neurotoxicology,* vol. 15, p. 95—107, 1994.

[23] P. A. JANMEY, "The Cytoskeleton and Cell Signaling: Component Localization and Mechanical Coupling," *Physiological Reviews,* vol. 78, pp. 763-781, 1998.

[24] C. Dong, R. Skalak, K.-L. P. Sung, G. W. Schmid-Scho¨nbein and S. Chien, "Passive Deformation Analysis of Human Leukocytes," *Journal of Biomechanical Engineering,* vol. 110, pp. 27-36, 2 1988.

[25] A. Yeung and E. Evans, "Cortical shell-liquid core model for passive flow of liquid-like spherical cells into micropipets," *Biophysical Journal,* vol. 56, pp. 139-149, 1989.

[26] A. J. Engler, S. Sen, H. L. Sweeney and D. E. Discher, "Matrix Elasticity Directs Stem Cell Lineage Specification," *Cell,* vol. 126, pp. 677-689, 2006.

[27] W. Yu, S. Sharma, J. K. Gimzewski and J. Rao, "Nanocytology as a potential biomarker for cancer," *Biomarkers in Medicine,* vol. 11, pp. 213-216, 2017.

[28] D. D. Carlo, "A Mechanical Biomarker of Cell State in Medicine," *Journal of Laboratory Automation,* vol. 17, pp. 32-42, 2012.

[29] D. R. Gossett, H. T. K. Tse, S. A. Lee, Y. Ying, A. G. Lindgren, O. O. Yang, J. Rao, A. T. Clark and D. Di Carlo, "Hydrodynamic stretching of single cells for large population mechanical phenotyping," *Proceedings of the National Academy of Sciences,* vol. 109, p. 7630–7635, 2012.

[30] R. Krishnan, J.-A. Park, C. Y. Seow, P. V.-S. Lee and A. G. Stewart, "Cellular Biomechanics in Drug Screening and Evaluation: Mechanopharmacology," *Trends in Pharmacological Sciences,* vol. 37, pp. 87-100, 2016.

[31] K. Burton and D. L. Taylor, "Traction forces of cytokinesis measured with optically modified elastic substrata," *Nature,* vol. 385, p. 450–454, 1997.

[32] M. F. Fournier, R. Sauser, D. Ambrosi, J.-J. Meister and A. B. Verkhovsky, "Force transmission in migrating cells," *Journal of Cell Biology,* vol. 188, pp. 287-297, 1 2010.

[33] C. N. Hall, C. Reynell, B. Gesslein, N. B. Hamilton, A. Mishra, B. A. Sutherland, F. M. O'Farrell, A. M. Buchan, M. Lauritzen and D. Attwell, "Capillary pericytes regulate cerebral blood flow in health and disease," *Nature,* vol. 508, p. 55–60, 2014.

[34] E. Evans, A. Leung and D. Zhelev, "Synchrony of cell spreading and contraction force as phagocytes engulf large pathogens," *Journal of Cell Biology,* vol. 122, pp. 1295-1300, 9 1993.

[35] J. Wang, F. Lin, Z. Wan, X. Sun, Y. Lu, J. Huang, F. Wang, Y. Zeng, Y.-H. Chen, Y. Shi, W. Zheng, Z. Li, C. Xiong and W. Liu, "Profiling the origin, dynamics, and function of traction force in B cell activation," *Sci. Signal.,* vol. 11, p. eaai9192, 8 2018.

[36] E. Bastounis, R. Meili, B. Álvarez-González, J. Francois, J. C. del Álamo, R. A. Firtel and J. C. Lasheras, "Both contractile axial and lateral traction force dynamics drive amoeboid cell motility," *Journal of Cell Biology,* vol. 204, pp. 1045-1061, 3 2014.

[37] S. Khan and M. P. Sheetz, "FORCE EFFECTS ON BIOCHEMICAL KINETICS," *Annual Review of Biochemistry,* vol. 66, pp. 785-805, 1997.

[38] E. Evans and A. Yeung, "Apparent viscosity and cortical tension of blood granulocytes determined by micropipet aspiration," *Biophysical Journal,* vol. 56, pp. 151-160, 1989.

[39] D. V. Zhelev and R. M. Hochmuth, "Mechanically stimulated cytoskeleton rearrangement and cortical contraction in human neutrophils," *Biophysical Journal,* vol. 68, pp. 2004-2014, 1995.

[40] A. J. Maniotis, C. S. Chen and D. E. Ingber, "Demonstration of mechanical connections between integrins, cytoskeletal filaments, and nucleoplasm that stabilize nuclear structure," *Proceedings of the National Academy of Sciences,* vol. 94, p. 849–854, 1997.

[41] D. J. Odde, L. Ma, A. H. Briggs, A. DeMarco and M. W. Kirschner, "Microtubule bending and breaking in living fibroblast cells.," *Journal of cell science,* vol. 112 (Pt 19), pp. 3283-8, 10 1999.

[42] M. Li, D. Dang, L. Liu, N. Xi and Y. Wang, "Atomic Force Microscopy in Characterizing Cell Mechanics for Biomedical Applications: A Review," *IEEE Transactions on NanoBioscience,* vol. 16, p. 523–540, 9 2017.

[43] J. J. Tomasek, G. Gabbiani, B. Hinz, C. Chaponnier and R. A. Brown, "Myofibroblasts and mechano-regulation of connective tissue remodelling," *Nature Reviews Molecular Cell Biology,* vol. 3, p. 349–363, 2002.

[44] N. M. Biel, K. E. Santostefano, B. B. DiVita, N. El Rouby, S. D. Carrasquilla, C. Simmons, M. Nakanishi, R. M. Cooper-DeHoff, J. A. Johnson and N. Terada, "Vascular Smooth Muscle Cells From Hypertensive Patient-Derived Induced Pluripotent Stem Cells to Advance Hypertension Pharmacogenomics," *STEM CELLS Translational Medicine,* vol. 4, pp. 1380-1390, 2015.

[45] M. Luo, K. Ni, P. Yu, Y. Jin, L. Liu, J. Li, Y. Pan and L. Deng, "Sanguinarine Decreases Cell Stiffness and Traction Force and Inhibits the Reactivity of Airway Smooth Muscle Cells in Culture," *Molecular & Cellular Biomechanics,* vol. 16, p. 141–151, 2019.

[46] C. Chen, R. Krishnan, E. Zhou, A. Ramachandran, D. Tambe, K. Rajendran, R. M. Adam, L. Deng and J. J. Fredberg, "Fluidization and Resolidification of the Human Bladder

Smooth Muscle Cell in Response to Transient Stretch," *PLOS ONE,* vol. 5, p. e12035, 8 2010.

[47] B. Li, M. Lin, Y. Tang, B. Wang and J. H.-C. Wang, "A novel functional assessment of the differentiation of micropatterned muscle cells," *Journal of Biomechanics,* vol. 41, pp. 3349-3353, 2008.

[48] S. R. Clippinger, P. E. Cloonan, L. Greenberg, M. Ernst, W. T. Stump and M. J. Greenberg, "Disrupted mechanobiology links the molecular and cellular phenotypes in familial dilated cardiomyopathy," *Proceedings of the National Academy of Sciences,* vol. 116, p. 17831–17840, 2019.

[49] H. Wu, H. Yang, J.-W. Rhee, J. Z. Zhang, C. K. Lam, K. Sallam, A. C. Y. Chang, N. Ma, J. Lee, H. Zhang, H. M. Blau, D. M. Bers and J. C. Wu, "Modelling diastolic dysfunction in induced pluripotent stem cell-derived cardiomyocytes from hypertrophic cardiomyopathy patients," *European Heart Journal,* vol. 40, pp. 3685-3695, 6 2019.

[50] H. Wu, J. Lee, L. Vincent, Q. Wang, M. Gu, F. Lan, J. Churko, K. Sallam, E. Matsa, A. Sharma, J. Gold, A. Engler, Y. Xiang, D. Bers and J. Wu, "Epigenetic Regulation of Phosphodiesterases 2A and 3A Underlies Compromised β-Adrenergic Signaling in an iPSC Model of Dilated Cardiomyopathy," *Cell Stem Cell,* vol. 17, pp. 89-100, 2015.

[51] A. Tanaka, S. Yuasa, K. Node and K. Fukuda, "Cardiovascular Disease Modeling Using Patient-Specific Induced Pluripotent Stem Cells," *International Journal of Molecular Sciences,* vol. 16, p. 18894–18922, 2015.

[52] C. Y. Park, E. H. Zhou, D. Tambe, B. Chen, T. Lavoie, M. Dowell, A. Simeonov, D. J. Maloney, A. Marinkovic, D. J. Tschumperlin, S. Burger, M. Frykenberg, J. P. Butler, W. D. Stamer, M. Johnson, J. Solway, J. J. Fredberg and R. Krishnan, "High-throughput screening for modulators of cellular contractile force," *Integrative Biology*, vol. 7, pp. 1318-1324, 5 2015.

[53] J. C. del Álamo, D. Lemons, R. Serrano, A. Savchenko, F. Cerignoli, R. Bodmer and M. Mercola, "High throughput physiological screening of iPSC-derived cardiomyocytes for drug development," *Biochimica et Biophysica Acta (BBA) - Molecular Cell Research*, vol. 1863, pp. 1717-1727, 2016.

[54] D. T. Paik, M. Chandy and J. C. Wu, "Patient and Disease–Specific Induced Pluripotent Stem Cells for Discovery of Personalized Cardiovascular Drugs and Therapeutics," *Pharmacological Reviews*, vol. 72, p. 320–342, 2020.

[55] A. A. N. Bruyneel, W. L. McKeithan, D. A. M. Feyen and M. Mercola, "Using iPSC Models to Probe Regulation of Cardiac Ion Channel Function," *Current Cardiology Reports*, vol. 20, p. 57, 2018.

[56] E. Karbassi, A. Fenix, S. Marchiano, N. Muraoka, K. Nakamura, X. Yang and C. E. Murry, "Cardiomyocyte maturation: advances in knowledge and implications for regenerative medicine," *Nature Reviews Cardiology*, vol. 17, p. 341–359, 2020.

[57] M. J. Birket, M. C. Ribeiro, A. O. Verkerk, D. Ward, A. R. Leitoguinho, S. C. den Hartogh, V. V. Orlova, H. D. Devalla, V. Schwach, M. Bellin, R. Passier and C. L.

Mummery, "Expansion and patterning of cardiovascular progenitors derived from human pluripotent stem cells," *Nature Biotechnology,* vol. 33, p. 970–979, 2015.

[58] Y. Shiba, T. Gomibuchi, T. Seto, Y. Wada, H. Ichimura, Y. Tanaka, T. Ogasawara, K. Okada, N. Shiba, K. Sakamoto, D. Ido, T. Shiina, M. Ohkura, J. Nakai, N. Uno, Y. Kazuki, M. Oshimura, I. Minami and U. Ikeda, "Allogeneic transplantation of iPS cell-derived cardiomyocytes regenerates primate hearts," *Nature,* vol. 538, p. 388–391, 2016.

[59] A. Ashkin, J. M. Dziedzic, J. E. Bjorkholm and S. Chu, "Observation of a single-beam gradient force optical trap for dielectric particles," *Opt. Lett.,* vol. 11, p. 288–290, 5 1986.

[60] S. N. S. Reihani and L. B. Oddershede, "Improving optical trapping in the axial direction and a continuous change of the optimal trapping depth," in *Optical Trapping and Optical Micromanipulation IV*, 2007.

[61] S. B. Smith, Y. Cui and C. Bustamante, "[7] Optical-trap force transducer that operates by direct measurement of light momentum," in *Biophotonics, Part B*, vol. 361, Academic Press, 2003, pp. 134-162.

[62] Z. Bryant, M. D. Stone, J. Gore, S. B. Smith, N. R. Cozzarelli and C. Bustamante, "Structural transitions and elasticity from torque measurements on DNA," *Nature,* vol. 424, p. 338–341, 2003.

[63] K. Berg-Sørensen and H. Flyvbjerg, "Power spectrum analysis for optical tweezers," *Review of Scientific Instruments,* vol. 75, p. 594–612, 3 2004.

[64] P. M. Hansen, I. M. Tolic-Nørrelykke, H. Flyvbjerg and K. Berg-Sørensen, "tweezercalib 2.1: Faster version of MatLab package for precise calibration of optical tweezers," *Computer Physics Communications,* vol. 175, pp. 572-573, 2006.

[65] R. M. Simmons, J. T. Finer, S. Chu and J. A. Spudich, "Quantitative measurements of force and displacement using an optical trap," *Biophysical Journal,* vol. 70, pp. 1813-1822, 1996.

[66] E.-L. Florin, A. Pralle, E. H. K. Stelzer and J. K. H. Hörber, "Photonic force microscope calibration by thermal noise analysis," *Applied Physics A,* vol. 66, p. S75–S78, 1998.

[67] A. Farré and M. Montes-Usategui, "A force detection technique for single-beam optical traps based on direct measurement of light momentum changes," *Opt. Express,* vol. 18, p. 11955–11968, 5 2010.

[68] M. Mahamdeh and E. Schäffer, "Optical tweezers with millikelvin precision of temperature-controlled objectives and base-pair resolution," *Opt. Express,* vol. 17, p. 17190–17199, 9 2009.

[69] M. Bussonnier, K. Carvalho, J. Lemière, J.-F. Joanny, C. Sykes and T. Betz, "Mechanical Detection of a Long-Range Actin Network Emanating from a Biomimetic Cortex," *Biophysical Journal,* vol. 107, pp. 854-862, 2014.

[70] J. Peukes and T. Betz, "Direct Measurement of the Cortical Tension during the Growth of Membrane Blebs," *Biophysical Journal,* vol. 107, pp. 1810-1820, 2014.

[71] J. Mas, A. C. Richardson, S. N. S. Reihani, L. B. Oddershede and K. Berg-Sørensen, "Quantitative determination of optical trapping strength and viscoelastic moduli inside living cells," *Physical Biology,* vol. 10, p. 046006, 7 2013.

[72] N. Chenouard, I. Smal, F. de Chaumont, M. Maška, I. F. Sbalzarini, Y. Gong, J. Cardinale, C. Carthel, S. Coraluppi, M. Winter, A. R. Cohen, W. J. Godinez, K. Rohr, Y. Kalaidzidis, L. Liang, J. Duncan, H. Shen, Y. Xu, K. E. G. Magnusson, J. Jaldén, H. M. Blau, P. Paul-Gilloteaux, P. Roudot, C. Kervrann, F. Waharte, J.-Y. Tinevez, S. L. Shorte, J. Willemse, K. Celler, G. P. van Wezel, H.-W. Dan, Y.-S. Tsai, C. O. de Solórzano, J.-C. Olivo-Marin and E. Meijering, "Objective comparison of particle tracking methods," *Nature Methods,* vol. 11, p. 281–289, 2014.

[73] S. F. Tolić-Nørrelykke, E. Schäffer, J. Howard, F. S. Pavone, F. Jülicher and H. Flyvbjerg, "Calibration of optical tweezers with positional detection in the back focal plane," *Review of Scientific Instruments,* vol. 77, p. 103101, 2006.

[74] A. R. Bausch, W. Möller and E. Sackmann, "Measurement of Local Viscoelasticity and Forces in Living Cells by Magnetic Tweezers," *Biophysical Journal,* vol. 76, p. 573–579, 1 1999.

[75] F. Amblard, B. Yurke, A. Pargellis and S. Leibler, "A magnetic manipulator for studying local rheology and micromechanical properties of biological systems," *Review of Scientific Instruments,* vol. 67, p. 818–827, 3 1996.

[76] M. P. De-Morales, M. Grabulosa, J. Alcaraz, J. Mullol, G. N. Maksym, J. J. Fredberg and D. Navajas, "Measurement of cell microrheology by magnetic twisting cytometry with

frequency domain demodulation," *Journal of Applied Physiology,* vol. 91, p. 1152–1159, 9 2001.

[77] P. Kollmannsberger and B. Fabry, "BaHigh-force magnetic tweezers with force feedback for biological applications," *Review of Scientific Instruments,* vol. 78, p. 114301, 11 2007.

[78] I. D. Vlaminck and C. Dekker, "Recent Advances in Magnetic Tweezers," *Annual Review of Biophysics,* vol. 41, p. 453–472, 6 2012.

[79] F. ALENGHAT, S. NAULI, K. O. L. B. R, Z. H. O. U. J and D. INGBER, "Global cytoskeletal control of mechanotransduction in kidney epithelial cells," *Experimental Cell Research,* vol. 301, p. 23–30, 11 2004.

[80] G. Massiera, K. M. V. Citters, P. L. Biancaniello and J. C. Crocker, "Mechanics of Single Cells: Rheology, Time Dependence, and Fluctuations," *Biophysical Journal,* vol. 93, p. 3703–3713, 11 2007.

[81] N. Wang, J. Butler and D. Ingber, "Mechanotransduction across the cell surface and through the cytoskeleton," *Science,* vol. 260, p. 1124–1127, 5 1993.

[82] S. Hu, L. Eberhard, J. Chen, J. C. Love, J. P. Butler, J. J. Fredberg, G. M. Whitesides and N. Wang, "Mechanical anisotropy of adherent cells probed by a three-dimensional magnetic twisting device," *American Journal of Physiology-Cell Physiology,* vol. 287, p. C1184–C1191, 11 2004.

[83] J.-Y. Tinevez, N. Perry, J. Schindelin, G. M. Hoopes, G. D. Reynolds, E. Laplantine, S. Y. Bednarek, S. L. Shorte and K. W. Eliceiri, "TrackMate: An open and extensible platform for single-particle tracking," *Methods,* vol. 115, p. 80–90, 2 2017.

[84] S. M. Mijailovich, M. Kojic, M. Zivkovic, B. Fabry and J. J. Fredberg, "A finite element model of cell deformation during magnetic bead twisting," *Journal of Applied Physiology,* vol. 93, p. 1429–1436, 10 2002.

[85] W. W. Ahmed, É. Fodor and T. Betz, "Active cell mechanics: Measurement and theory," *Biochimica et Biophysica Acta (BBA) - Molecular Cell Research,* vol. 1853, p. 3083–3094, 11 2015.

[86] M. L. Rodriguez, P. J. McGarry and N. J. Sniadecki, "Review on Cell Mechanics: Experimental and Modeling Approaches," *Applied Mechanics Reviews,* vol. 65, 10 2013.

[87] P. Kollmannsberger and B. Fabry, "Linear and Nonlinear Rheology of Living Cells," *Annual Review of Materials Research,* vol. 41, p. 75–97, 8 2011.

[88] M. Radmacher, R. Tillamnn, M. Fritz and H. Gaub, "From molecules to cells: imaging soft samples with the atomic force microscope," *Science,* vol. 257, p. 1900–1905, 9 1992.

[89] M. Radmacher, R. W. Tillmann and H. E. Gaub, "Imaging viscoelasticity by force modulation with the atomic force microscope," *Biophysical Journal,* vol. 64, p. 735–742, 3 1993.

[90] M. Radmacher, "Studying the Mechanics of Cellular Processes by Atomic Force Microscopy," in *Methods in Cell Biology*, Elsevier, 2007, p. 347–372.

[91] P. I. Chang, P. Huang, J. Maeng and S. B. Andersson, "Local raster scanning for high-speed imaging of biopolymers in atomic force microscopy," *Review of Scientific Instruments*, vol. 82, p. 063703, 6 2011.

[92] M. Lekka, D. Gil, K. Pogoda, J. Dulińska-Litewka, R. Jach, J. Gostek, O. Klymenko, S. Prauzner-Bechcicki, Z. Stachura, J. Wiltowska-Zuber, K. Okoń and P. Laidler, "Cancer cell detection in tissue sections using AFM," *Archives of Biochemistry and Biophysics*, vol. 518, p. 151–156, 2 2012.

[93] D. J. Müller and Y. F. Dufrêne, "Force nanoscopy of living cells," *Current Biology*, vol. 21, p. R212–R216, 3 2011.

[94] J. Hardij, F. Cecchet, A. Berquand, D. Gheldof, C. Chatelain, F. Mullier, B. Chatelain and J.-M. Dogné, "Characterisation of tissue factor-bearing extracellular vesicles with AFM: comparison of air-tapping-mode AFM and liquid Peak Force AFM," *Journal of Extracellular Vesicles*, vol. 2, p. 21045, 1 2013.

[95] K. A. Ramirez-Aguilar and K. L. Rowlen, "Tip Characterization from AFM Images of Nanometric Spherical Particles," *Langmuir*, vol. 14, p. 2562–2566, 4 1998.

[96] H. Hertz, "Ueber die Berührung fester elastischer Körper," in *Journal für die reine und angewandte Mathematik Band 92*, De Gruyter, 1882, p. 156–171.

[97] I. N. Sneddon, "The relation between load and penetration in the axisymmetric boussinesq problem for a punch of arbitrary profile," *International Journal of Engineering Science,* vol. 3, p. 47–57, 5 1965.

[98] S. V. Kontomaris and A. Malamou, "Hertz model or Oliver & Pharr analysis? Tutorial regarding AFM nanoindentation experiments on biological samples," *Materials Research Express,* vol. 7, p. 033001, 3 2020.

[99] H. Schillers, I. Medalsy, S. Hu, A. L. Slade and J. E. Shaw, "PeakForce Tapping resolves individual microvilli on living cells," *Journal of Molecular Recognition,* vol. 29, p. 95–101, 9 2015.

[100] H. Yamashita, A. Taoka, T. Uchihashi, T. Asano, T. Ando and Y. Fukumori, "Single-Molecule Imaging on Living Bacterial Cell Surface by High-Speed AFM," *Journal of Molecular Biology,* vol. 422, p. 300–309, 9 2012.

[101] T. Ando, "High-speed AFM imaging," *Current Opinion in Structural Biology,* vol. 28, p. 63–68, 10 2014.

[102] R. E. Mahaffy, C. K. Shih, F. C. MacKintosh and J. Käs, "Scanning Probe-Based Frequency-Dependent Microrheology of Polymer Gels and Biological Cells," *Physical Review Letters,* vol. 85, p. 880–883, 7 2000.

[103] R. E. Mahaffy, S. Park, E. Gerde, J. Käs and C. K. Shih, "Quantitative Analysis of the Viscoelastic Properties of Thin Regions of Fibroblasts Using Atomic Force Microscopy," *Biophysical Journal,* vol. 86, p. 1777–1793, 3 2004.

[104] M. H. Korayem, M. B. Saraie and M. B. Saraee, "Analysis the effect of different geometries of AFM\textquotesingles cantilever on the dynamic behavior and the critical forces of three-dimensional manipulation," *Ultramicroscopy,* vol. 175, p. 9–24, 4 2017.

[105] N. Gavara, "A beginner\textquotesingles guide to atomic force microscopy probing for cell mechanics," *Microscopy Research and Technique,* vol. 80, p. 75–84, 9 2016.

[106] S. Sen, S. Subramanian and D. E. Discher, "Indentation and Adhesive Probing of a Cell Membrane with AFM: Theoretical Model and Experiments," *Biophysical Journal,* vol. 89, p. 3203–3213, 11 2005.

[107] T. Zmantar, F. Bettaieb, K. Chaieb, B. Ezzili, L. Mora-Ponsonnet, A. Othmane, N. Jaffrézic and A. Bakhrouf, "Atomic force microscopy and hydrodynamic characterization of the adhesion of staphylococcus aureus to hydrophilic and hydrophobic substrata at different pH values," *World Journal of Microbiology and Biotechnology,* vol. 27, p. 887–896, 8 2010.

[108] S. Park and Y. J. Lee, "AFM-based dual nano-mechanical phenotypes for cancer metastasis," *Journal of Biological Physics,* vol. 40, p. 413–419, 6 2014.

[109] J. Liu, N. Sun, M. A. Bruce, J. C. Wu and M. J. Butte, "Atomic Force Mechanobiology of Pluripotent Stem Cell-Derived Cardiomyocytes," *PLoS ONE,* vol. 7, p. e37559, 5 2012.

[110] N. E. Oyunbaatar, D. S. Kim, E. S. Kim, B. K. Lee and D. W. Lee, "Cardiac toxicity screening using polymeric cantilever integrated with cell stimulators," in *2017 IEEE 30th International Conference on Micro Electro Mechanical Systems (MEMS)*, 2017.

[111] P. P. Kanade, N.-E. Oyunbaatar and D.-W. Lee, "Polymer-Based Functional Cantilevers Integrated with Interdigitated Electrode Arrays—A Novel Platform for Cardiac Sensing," *Micromachines,* vol. 11, p. 450, 4 2020.

[112] K. E. Steucke, P. V. Tracy, E. S. Hald, J. L. Hall and P. W. Alford, "Vascular smooth muscle cell functional contractility depends on extracellular mechanical properties," *Journal of Biomechanics,* vol. 48, p. 3044–3051, 9 2015.

[113] T. Beléndez, C. Neipp and A. Beléndez, "Large and small deflections of a cantilever beam," *European Journal of Physics,* vol. 23, p. 371–379, 5 2002.

[114] B. B. Muvdi and J. W. McNabb, "Stress, Strain, and Their Relationships," in *Engineering Mechanics of Materials*, Springer New York, 1991, p. 60–120.

[115] O. du Roure, C. Dequidt, A. Richert, R. H. Austin, A. Buguin, P. Chavrier, P. Silberzan and B. Ladoux, "Microfabricated arrays of elastomeric posts to study cellular mechanics," in *Microfluidics, BioMEMS, and Medical Microsystems II*, 2003.

[116] M. Ghibaudo, A. Saez, L. Trichet, A. Xayaphoummine, J. Browaeys, P. Silberzan, A. Buguin and B. Ladoux, "Traction forces and rigidity sensing regulate cell functions," *Soft Matter,* vol. 4, no. 9, pp. 1836-1843, 2008.

[117] A. Saez, E. Anon, M. Ghibaudo, O. du Roure, J.-M. D. Meglio, P. Hersen, P. Silberzan, A. Buguin and B. Ladoux, "Traction forces exerted by epithelial cell sheets," *Journal of Physics: Condensed Matter,* vol. 22, p. 194119, 4 2010.

[118] K. A. Addae-Mensah, N. J. Kassebaum, M. J. Bowers, R. S. Reiserer, S. J. Rosenthal, P. E. Moore and J. P. Wikswo, "A flexible, quantum dot-labeled cantilever post array for studying cellular microforces," *Sensors and Actuators A: Physical,* vol. 136, pp. 385-397, 2007.

[119] B. Sabass, M. L. Gardel, C. M. Waterman and U. S. Schwarz, "High Resolution Traction Force Microscopy Based on Experimental and Computational Advances," *Biophysical Journal,* vol. 94, pp. 207-220, 2008.

[120] D. Vorselen, Y. Wang, M. M. de Jesus, P. K. Shah, M. J. Footer, M. Huse, W. Cai and J. A. Theriot, "Microparticle traction force microscopy reveals subcellular force exertion patterns in immune cell–target interactions," *Nature Communications,* vol. 11, 1 2020.

[121] H. Nobach and M. Honkanen, "Two-dimensional Gaussian regression for sub-pixel displacement estimation in particle image velocimetry or particle position estimation in particle tracking velocimetry," *Experiments in Fluids,* vol. 38, p. 511–515, 3 2005.

[122] X. Trepat, M. R. Wasserman, T. E. Angelini, E. Millet, D. A. Weitz, J. P. Butler and J. J. Fredberg, "Physical forces during collective cell migration," *Nature Physics,* vol. 5, p. 426–430, 2009.

[123] R. Rokhzan, C. C. Ghosh, N. Schaible, J. Notbohm, H. Yoshie, A. J. Ehrlicher, S. J. Higgins, R. Zhang, H. Haller, C. C. Hardin, S. David, S. M. Parikh and R. Krishnan, "Multiplexed, high-throughput measurements of cell contraction and endothelial barrier function," *Laboratory Investigation,* vol. 99, p. 138–145, 2019.

[124] H. Yoshie, N. Koushki, R. Kaviani, M. Tabatabaei, K. Rajendran, Q. Dang, A. Husain, S. Yao, C. Li, J. K. Sullivan, M. Saint-Geniez, R. Krishnan and A. J. Ehrlicher, "Traction Force Screening Enabled by Compliant PDMS Elastomers," *Biophysical Journal,* vol. 114, pp. 2194-2199, 2018.

[125] H. AU Yoshie, N. AU Koushki, C. AU Molter, P. M. AU Siegel, R. AU Krishnan and A. J. AU Ehrlicher, "High Throughput Traction Force Microscopy Using PDMS Reveals Dose-Dependent Effects of Transforming Growth Factor-β on the Epithelial-to-Mesenchymal Transition," *JoVE,* p. e59364, 2019.

[126] R. J. Jerrell and A. Parekh, "Cellular traction stresses mediate extracellular matrix degradation by invadopodia," *Acta Biomaterialia,* vol. 10, pp. 1886-1896, 2014.

[127] I. Pushkarsky, P. Tseng, D. Black, B. France, L. Warfe, C. J. Koziol-White, W. F. Jester, R. K. Trinh, J. Lin, P. O. Scumpia, S. L. Morrison, R. A. Panettieri, R. Damoiseaux and D. Di Carlo, "Elastomeric sensor surfaces for high-throughput single-cell force cytometry," *Nature Biomedical Engineering,* vol. 2, p. 124–137, 2018.

[128] J. Fu, Y.-K. Wang, M. T. Yang, R. A. Desai, X. Yu, Z. Liu and C. S. Chen, "Mechanical regulation of cell function with geometrically modulated elastomeric substrates," *Nature Methods,* vol. 7, p. 733–736, 8 2010.

[129] J. Lecoq, N. Orlova and B. F. Grewe, "Wide. Fast. Deep: Recent Advances in Multiphoton Microscopy of In Vivo Neuronal Activity," *Journal of Neuroscience,* vol. 39, p. 9042–9052, 2019.

[130] S. I. Protze, J. Liu, U. Nussinovitch, L. Ohana, P. H. Backx, L. Gepstein and G. M. Keller, "Sinoatrial node cardiomyocytes derived from human pluripotent cells function as a biological pacemaker," *Nature Biotechnology,* vol. 35, p. 56–68, 2017.

[131] A. M. da Rocha, J. Creech, E. Thonn, S. Mironov and T. J. Herron, "Detection of Drug-Induced Torsades de Pointes Arrhythmia Mechanisms Using hiPSC-CM Syncytial Monolayers in a High-Throughput Screening Voltage Sensitive Dye Assay," *Toxicological Sciences,* vol. 173, pp. 402-415, 11 2019.

[132] S. R. Braam, R. Passier and C. L. Mummery, "Cardiomyocytes from human pluripotent stem cells in regenerative medicine and drug discovery," *Trends in Pharmacological Sciences,* vol. 30, pp. 536-545, 2009.

[133] R. M. Smith, N. Suleman, L. Lacerda, L. H. Opie, S. Akira, K. R. Chien and M. N. Sack, "Genetic depletion of cardiac myocyte STAT-3 abolishes classical preconditioning," *Cardiovascular Research,* vol. 63, pp. 611-616, 9 2004.

[134] J. J. Saucerman, P. M. Tan, K. S. Buchholz, A. D. McCulloch and J. H. Omens, "Mechanical regulation of gene expression in cardiac myocytes and fibroblasts," *Nature Reviews Cardiology,* vol. 16, p. 361–378, 2019.

[135] S. Okumura, Y. Hirano, Y. Maki and Y. Komatsu, "Analysis of time-course drug response in rat cardiomyocytes cultured on a pattern of islands," *Analyst,* vol. 143, no. 17, pp. 4083-4089, 2018.

[136] A. Sharma, W. L. McKeithan, R. Serrano, T. Kitani, P. W. Burridge, J. C. del Álamo, M. Mercola and J. C. Wu, "Use of human induced pluripotent stem cell-derived cardiomyocytes to assess drug cardiotoxicity," *Nature Protocols,* vol. 13, p. 3018–3041, 2018.

[137] A. Gibbons, O. Lang, Y. Kojima, M. Ito, K. Ono, K. Tanaka and E. Sivaniah, "Real-time visualization of cardiac cell beating behaviour on polymer diffraction gratings," *RSC Adv.*, vol. 7, no. 81, pp. 51121-51129, 2017.

[138] B. T. Wyman, W. C. Hunter, F. W. Prinzen and E. R. McVeigh, "Mapping propagation of mechanical activation in the paced heart with MRI tagging," *American Journal of Physiology-Heart and Circulatory Physiology,* vol. 276, pp. H881-H891, 1999.

[139] F. S. Pasqualini, A. Agarwal, B. B. O\textquotesingleConnor, Q. Liu, S. P. Sheehy and K. K. Parker, "Traction force microscopy of engineered cardiac tissues," *PLOS ONE,* vol. 13, p. e0194706, 3 2018.

[140] S. Gargiulo, A. Greco, M. Gramanzini, M. P. Petretta, A. Ferro, M. Larobina, M. Panico, A. Brunetti and A. Cuocolo, "PET/CT Imaging in Mouse Models of Myocardial Ischemia," *Journal of Biomedicine and Biotechnology,* vol. 2012, p. 1–12, 2012.

[141] F. Xiao, X. Wen, X. H. M. Tan and P.-Y. Chiou, "Plasmonic micropillars for precision cell force measurement across a large field-of-view," *Applied Physics Letters,* vol. 112, p. 033701, 2018.

[142] Z. Wang, A. A. Volinsky and N. D. Gallant, "Crosslinking effect on polydimethylsiloxane elastic modulus measured by custom-built compression instrument," *Journal of Applied Polymer Science*, vol. 131, 2014.

[143] Z. Al-Rekabi and A. E. Pelling, "Cross talk between matrix elasticity and mechanical force regulates myoblast traction dynamics," *Physical Biology*, vol. 10, p. 066003, 10 2013.

[144] L. Zwi, O. Caspi, G. Arbel, I. Huber, A. Gepstein, I.-H. Park and L. Gepstein, "Cardiomyocyte Differentiation of Human Induced Pluripotent Stem Cells," *Circulation*, vol. 120, p. 1513–1523, 10 2009.

[145] Y. Feld, M. Melamed-Frank, I. Kehat, D. Tal, S. Marom and L. Gepstein, "Electrophysiological Modulation of Cardiomyocytic Tissue by Transfected Fibroblasts Expressing Potassium Channels," *Circulation*, vol. 105, p. 522–529, 1 2002.

[146] G. I. D. E. O. N. MEIRY, Y. O. T. A. M. REISNER, F. E. L. D. YAIR, S. T. A. N. I. S. L. A. V. GOLDBERG, M. I. C. H. A. E. L. ROSEN, Z. I. V. NOAM and O. F. E. R. BINAH, "Evolution of Action Potential Propagation and Repolarization in Cultured Neonatal Rat Ventricular Myocytes," *Journal of Cardiovascular Electrophysiology*, vol. 12, p. 1269–1277, 11 2001.

[147] H. Zhu, S. McElwee-Witmer, M. Perrone, K. L. Clark and A. Zilberstein, "Phenylephrine protects neonatal rat cardiomyocytes from hypoxia and serum deprivation-induced apoptosis," *Cell Death & Differentiation*, vol. 7, p. 773–784, 8 2000.

[148] A. M. Prasad, H. Ma, C. Sumbilla, D. I. Lee, M. G. Klein and G. Inesi, "Phenylephrine hypertrophy, Ca2\mathplus{}{-}{ATPase} (SERCA2), and Ca2\mathplus{}{s}{i}gnaling in neonatal rat cardiac myocytes," *American Journal of Physiology-Cell Physiology,* vol. 292, p. C2269–C2275, 6 2007.

[149] C. E. Rupert, H. H. Chang and K. L. K. Coulombe, "Hypertrophy Changes 3D Shape of hiPSC-Cardiomyocytes: Implications for Cellular Maturation in Regenerative Medicine," *Cellular and Molecular Bioengineering,* vol. 10, p. 54–62, 8 2016.

[150] N. J. Sniadecki, A. Anguelouch, M. T. Yang, C. M. Lamb, Z. Liu, S. B. Kirschner, Y. Liu, D. H. Reich and C. S. Chen, "Magnetic microposts as an approach to apply forces to living cells," *Proceedings of the National Academy of Sciences,* vol. 104, p. 14553–14558, 9 2007.

[151] P. Tseng, J. W. Judy and D. D. Carlo, "Magnetic nanoparticle–mediated massively parallel mechanical modulation of single-cell behavior," *Nature Methods,* vol. 9, p. 1113–1119, 10 2012.

[152] J. Rother, H. Nöding, I. Mey and A. Janshoff, "Atomic force microscopy-based microrheology reveals significant differences in the viscoelastic response between malign and benign cell lines," *Open Biology,* vol. 4, p. 140046, 5 2014.

[153] "Single-pixel optical technologies for instantly quantifying multicellular response profiles". Patent WO2019010234A1, 2019.

[154] D. E. Jaalouk and J. Lammerding, "Mechanotransduction gone awry," *Nature Reviews Molecular Cell Biology,* vol. 10, p. 63–73, 2009.

[155] P. Hersen and B. Ladoux, "Push it, pull it," *Nature,* vol. 470, p. 340–341, 2011.

[156] C. T. Lim, A. Bershadsky and M. P. Sheetz, "Mechanobiology," *Journal of The Royal Society Interface,* vol. 7, pp. S291-S293, 2010.

[157] S. Kumar and V. M. Weaver, "Mechanics, malignancy, and metastasis: The force journey of a tumor cell," *Cancer and Metastasis Reviews,* vol. 28, p. 113–127, 2009.

[158] K. C. Neuman and S. M. Block, "Optical trapping," *Review of Scientific Instruments,* vol. 75, pp. 2787-2809, 2004.